Liu *et al. Translational Neurodegeneration* (2026) 15:61
https://doi.org/10.1186/s40035-026-00595-9

Translational Neurodegeneration

RESEARCH

Open Access

Neuron-enriched STAT4 shapes time- and context-dependent neuronal outcomes in Alzheimer's disease

Junting Liu[1], Congcong Liu[1], Jing Liu[1], Yuli Hou[1], Jingrong Cao[1], Yujian Fan[1], Haixia Ma[1], Shuo Gao[1] and Peichang Wang[1*]

Abstract

Background Neuronal dysfunction in Alzheimer's disease (AD) is increasingly linked to dynamic and context-dependent alterations in intracellular signaling. However, how these changes drive progressive neurodegeneration and divergent neuronal outcomes remains poorly understood.

Methods Integrative analyses across independent human single-nucleus RNA sequencing datasets were performed to identify neuronal factors consistently altered in AD. Signal transducer and activator of transcription 4 (STAT4) distribution in different cell types was further validated using a mouse single-cell RNA sequencing dataset and experimental models. Functions of STAT4 were examined in human SH-SY5Y cells, mouse HT22 neuronal cells, mouse primary neurons, and inducible systems. In vivo effects were assessed in 3×Tg-AD and wild-type mice with AAV-mediated *Stat4* modulation and pharmacological ERK inhibition. Multi-omics approaches, including RNA-seq, Cut&Tag, and RIP-seq, were used to explore downstream regulatory mechanisms.

Results Integrative analyses identified STAT4 as a neuron-enriched factor consistently reduced in AD neurons. STAT4 supported neuronal integrity and synaptic homeostasis under basal conditions. Inducible restoration of STAT4 expression exerted divergent effects in a time-dependent manner, with early adaptive responses transitioning to later oxidative stress- and apoptosis-associated changes. Sustained STAT4 restoration induced oxidative stress, apoptosis-related signaling, and tau protein-related alterations, which were attenuated by ERK inhibition. In contrast, the beneficial outputs, including reduced Aβ burden and improved synaptic and neuronal markers, were preserved despite ERK inhibition. Parallel analyses in wild-type mice showed a delayed trajectory, indicating disease-context-dependent modulation. STAT4 was further associated with coordinated signaling networks and hnRNPK-related regulatory complexes.

Conclusions These findings define a time- and context-dependent signaling framework in which STAT4-associated outputs progressively shift toward maladaptive, ERK-sensitive responses in AD. Selective constraint of the late-stage signaling imbalance may attenuate the pathological outcomes while preserving the beneficial effects, providing a potential strategy for context-specific therapeutic intervention.

Keywords Alzheimer's disease, STAT4, Neuronal signaling, Time-dependent regulation, Context-dependent signaling, Synaptic homeostasis, HnRNPK

*Correspondence:
Peichang Wang
pcw1905@126.com
Full list of author information is available at the end of the article

© The Author(s) 2026. **Open Access** This article is licensed under a Creative Commons Attribution 4.0 International License, which permits use, sharing, adaptation, distribution and reproduction in any medium or format, as long as you give appropriate credit to the original author(s) and the source, provide a link to the Creative Commons licence, and indicate if changes were made. The images or other third party material in this article are included in the article's Creative Commons licence, unless indicated otherwise in a credit line to the material. If material is not included in the article's Creative Commons licence and your intended use is not permitted by statutory regulation or exceeds the permitted use, you will need to obtain permission directly from the copyright holder. To view a copy of this licence, visit http://creativecommons.org/licenses/by/4.0/. The Creative Commons Public Domain Dedication waiver (http://creativecommons.org/publicdomain/zero/1.0/) applies to the data made available in this article, unless otherwise stated in a credit line to the data.

Introduction

AD is characterized by progressive neuronal dysfunction [1–3], accompanied by widespread alterations in intracellular signaling. Increasing evidence suggests that these signaling changes are not uniform but instead show marked context dependence [4–6], with the same pathways producing distinct outputs depending on cellular state, disease stage, and environmental conditions. However, how such context-dependent signaling outputs are temporally coordinated in neurons remains poorly understood.

A related challenge is that neuronal signaling can give rise to divergent functional outputs, including both adaptive and maladaptive responses [7–10]. While such opposing effects have been described in multiple systems, the mechanisms that determine when and how these transitions occur remain unclear, particularly in neurodegenerative disease. Addressing this question requires approaches that capture both cell-type specificity and dynamic changes over time [11–13].

Members of the signal transducer and activator of transcription (STAT) family are well known for their roles in immune regulation, but emerging evidence suggests that they may also participate in neuronal processes [14–16]. Among them, STAT4 has been extensively studied in immune cells [17–19] but remains largely unexplored in the nervous system and in AD. Whether STAT4 contributes to neuronal function and how it behaves under disease conditions are unknown. Recent advances in single-cell [20–22] and multi-omics [23, 24] technologies, together with experimental systems that enable temporal control of gene expression [25], provide an opportunity to identify candidate regulators and examine their dynamic behavior in disease-relevant contexts.

In this study, we identify STAT4 as a neuron-associated regulator that is reduced in AD and required for maintaining neuronal integrity. We show that STAT4 supports neuronal and synaptic homeostasis and engages both PI3K/AKT and MAPK/ERK signaling pathways, suggesting a dual-output regulatory architecture. In the context of AD, however, this signaling balance becomes progressively disrupted, resulting in ERK-biased maladaptive output although the beneficial downstream effects are preserved. We further show that pharmacologic inhibition of ERK can constrain this maladaptive component while retaining the beneficial effects of STAT4 restoration. These findings establish a framework in which STAT4 functions not as a uniformly protective or pathogenic factor, but as a context-dependent regulator of neuronal homeostasis whose therapeutic modulation in AD may require concurrent ERK constraint.

Materials and methods

Antibodies, reagents and commercial kits

All antibodies used in this study are provided in Table S1. All reagents, chemicals, and commercial kits used in this study, including catalog numbers and sources, are summarized in Table S2. To facilitate tracking of the experimental systems used throughout the study, the datasets, species, animal models, the analysis purpose of their use, corresponding figures, and weblinks or sources are summarized in Table S3.

Public datasets and bioinformatic analyses

Public datasets

Publicly available transcriptomic datasets were obtained from the Gene Expression Omnibus (GEO). Three human single-nucleus RNA sequencing (snRNA-seq) datasets, GSE222007, GSE188545, and GSE157827, were used to identify neuronal genes consistently downregulated in AD. These datasets were also used to compare *STAT4* expression between AD and control neuronal populations. The human snRNA-seq dataset GSE222007 was further used to assess the distribution of *STAT4* expression across major cell types in brain. To validate STAT4 distribution in different cell types in mouse models of disease, the mouse single-cell RNA sequencing (scRNA-seq) dataset GSE261596, generated from brain tissues of 3×Tg-AD mice and corresponding WT mice, was analyzed. For downstream network and correlation analyses, bulk RNA-seq data from GSE203206 were used for weighted gene co-expression network analysis (WGCNA), whereas GSE159699 and GSE203206 were used for correlation analyses between *STAT4* and genes of interest.

Differential expression consistently found across neuronal datasets

To identify neuronal genes consistently downregulated in AD, three independent human snRNA-seq datasets were analyzed, including GSE222007, GSE188545, and GSE157827. In each dataset, genes downregulated in AD neurons relative to control neurons were collected according to the predefined differential expression criteria. Overlap of downregulated neuronal genes across the three datasets was visualized using a Venn diagram. Candidate genes showing convergent downregulation across independent human neuronal snRNA-seq datasets were prioritized for further analysis. Based on this analysis, *STAT4* was selected as a candidate gene for subsequent validation and functional investigation.

WGCNA

WGCNA [26, 27] was performed using the R package WGCNA on bulk RNA-seq data from GSE203206. Genes with low expression or low variance were removed before network construction according to standard preprocessing criteria. A soft-thresholding power of $\beta = 26$ was selected to approximate scale-free topology. An adjacency matrix was then transformed into a topological overlap matrix, followed by hierarchical clustering and dynamic tree cutting to define gene modules. Module eigengenes were calculated and correlated with AD-related traits. The turquoise module was selected for downstream visualization and interpretation based on its association with AD-related traits and enrichment in signaling-related genes. Intramodular hub genes were defined according to module membership ($|KME| \geq 0.8$). KEGG pathway annotations were used to assess the enrichment of PI3K/RAS/MAPK-related signaling components.

Correlation analyses in public human datasets

Expression correlations between *STAT4* and genes of interest were evaluated in GSE159699, GSE203206, and GTEx datasets as indicated in the following Results section. Correlation coefficients were calculated using Pearson or Spearman analysis as appropriate based on data distribution. For GTEx-based analyses, BA9 cortex and hippocampus datasets were used to assess the relationship between *STAT4* and neuronal/synaptic marker genes.

Animals and experimental design

Male 3×Tg-AD mice and age-matched C57BL/6J wild-type (WT) controls were obtained from Beijing Weishanglide Biotechnology Co., Ltd (Beijing, China). Male 5×FAD mice and age-matched WT controls were used for validation of STAT4 localization and expression patterns. Mice were housed under a 12-h light/dark cycle at 23 °C with ad libitum access to food and water. All animal procedures were approved by the Animal Care and Use Committee of Xuanwu Hospital, Capital Medical University, and were performed in accordance with institutional guidelines and the regulations of the Chinese Administration of Laboratory Animals.

For the main in vivo intervention study, 5-month-old 3×Tg-AD mice and age-matched WT mice underwent stereotactic hippocampal injection of adeno-associated virus (AAV) vectors for *Stat4* overexpression or vector control, which were provided by Shanghai GeneChem Co., Ltd. (Shanghai, China). The age of 5 months was selected based on our preliminary observation that endogenous STAT4 reduction became evident by 6 months. Therefore, this timeline allows intervention to be initiated before significant downregulation was detected. The effects of *Stat4* overexpression were evaluated at 4 and 8 weeks after AAV injection, to represent short-term and long-term effects, respectively. PD0325901 (PDi; 10 mg/kg [28]) was prepared in vehicle consisting of 0.5% hydroxypropyl methylcellulose (HPMC) and 0.2% Tween 80 and administered by oral gavage every 4 days during weeks 4–8 after AAV injection. This yielded four 8-week groups in 3×Tg-AD mice: vector + vehicle, vector + PDi, STAT4 + vehicle, and STAT4 + PDi. In parallel, WT mice receiving *Stat4* overexpression or vector control were assessed at 4, 8, and 12 weeks after AAV injection to examine the temporal profile of STAT4-associated effects in a non-AD background.

Group sizes were 8–10 mice per group for most WT groups and 3×Tg-AD groups. Unless otherwise stated, sample sizes for each experiment are provided in the corresponding figure legends.

Stereotaxic hippocampal injection

To achieve neuron-biased expression of STAT4 in the hippocampus, an AAV serotype AAV-PHP.eB was used. The *Stat4* overexpression construct was AAV-hSyn-Stat4(K24K0126)-EGFP, which contained the mouse STAT4 coding sequence driven by the human synapsin (hSyn) promoter. The control vector was AAV-hSyn-EGFP. Viral particles were generated by Shanghai GeneChem Co., Ltd. (Shanghai, China) and used at a final titer of 1.0×10^{13} vg/mL.

Mice were anesthetized with tribromoethanol and placed in a stereotaxic apparatus. Viral suspension (1.0 μL per side) was bilaterally injected into the hippocampus using the following coordinates relative to bregma: anteroposterior (AP), −2.50 mm; mediolateral (ML), ±2.00 mm; dorsoventral (DV), −1.80 mm. Injection was performed according to standard stereotaxic procedures by experienced personnel. After injection, mice were returned to their home cages for recovery and monitored routinely. Transgene expression was verified by EGFP fluorescence and/or STAT4 immunostaining in the hippocampus.

Behavioral testing

Behavioral testing was performed during the daytime light phase in a dedicated behavioral room under controlled environmental conditions. Mice were habituated to the testing room before each session. Behavioral data were collected using the Smart 3.0 video tracking system and analyzed according to predefined scoring criteria.

Novel object recognition (NOR)

NOR testing was performed as previously described [29] with minor modifications. Mice were tested at 4, 8, and 12 weeks after AAV injection. The test consisted of three phases: adaptation, familiarization, and testing. During adaptation, mice were individually placed in an empty open-field arena for 5 min per day for 2–3 consecutive days. During familiarization, mice were allowed to explore two identical objects for 5 min. Twenty-four hours later, one familiar object was replaced with a novel object, and mice were allowed to explore for 5 min.

Behavior was recorded using the Smart 3.0 video tracking system. Active exploration was defined as the nose being within 2 cm of the object and oriented toward it; sitting on or passing by an object without active investigation was not counted as exploration. Novel object preference was calculated as follows: Novel object preference (%) = [time exploring the novel object/(time exploring the novel object + time exploring the familiar object)] × 100%. Apparatuses and objects were cleaned with alcohol between trials to eliminate olfactory cues.

Morris water maze (MWM)

The MWM test was conducted as described previously [30]. The apparatus consisted of a circular pool (90 cm in diameter) filled with opaque water maintained at 22 °C. Visual cues were placed around the room. The task included visible platform training, hidden platform training, and the probe test.

During visible platform training (1–2 days), the platform was positioned above the water surface and marked with a visible flag to assess sensorimotor function and habituation. During hidden platform training (5 days), the platform was submerged approximately 1 cm below the water surface in the northeast quadrant. Each mouse underwent four trials per day with four different starting points in pseudorandom order. The maximum trial duration was 60 s. Mice that failed to locate the platform within 60 s were guided to the platform and allowed to remain there briefly. Escape latency was recorded as the primary learning measure. On the day following hidden platform training, the platform was removed and a probe test was performed. Mice were introduced from the quadrant opposite to the target quadrant, and the time spent in the target quadrant and the number of platform crossings were recorded.

Cell culture and lentiviral transduction

Laboratory-maintained SH-SY5Y and HT22 cells were cultured in Dulbecco's modified Eagle's medium (DMEM; VivaCell Biosciences, Shanghai, China) supplemented with 10% fetal bovine serum at 37 °C in a humidified incubator with 5% CO_2, as described previously [29, 31].

Lentiviral constructs, including conventional *STAT4/Stat4* overexpression vectors, *STAT4/Stat4* knockdown vectors, Tet-On inducible *Stat4* overexpression constructs, *hnRNPK* knockdown vectors, and corresponding control vectors, were synthesized by Shanghai GeneChem Co., Ltd. (Shanghai, China). For *STAT4/Stat4* overexpression constructs, the inserted coding sequence was human *STAT4* for SH-SY5Y cells and mouse *Stat4* for HT22 cells and primary neurons. All constructs contained a puromycin resistance cassette for stable selection where applicable.

For SH-SY5Y and HT22 cells, lentiviral transduction was performed at multiplicities of infection (MOIs) of 40 and 20, respectively. Stable SH-SY5Y and HT22 cell lines were selected with puromycin at 1.5 and 2 μg/mL, respectively. For primary neurons, lentiviral transduction was performed at an MOI of 80 without puromycin selection. Cells were incubated with lentivirus for 48 h before medium replacement. For Tet-On experiments, *Stat4* expression was induced with doxycycline at 0.5 μg/mL for the indicated durations. Overexpression or knockdown efficiency was validated by quantitative PCR and Western blotting before downstream experiments.

Primary neuronal culture and Aβ treatment

Primary cortical neurons were prepared from fetal WT mice obtained from pregnant mice 2–3 days before the expected date of delivery. Neuronal isolation and culture were performed using a mouse cortical neuron isolation and culture kit (P-CA-704; Procell Life Science & Technology Co., Ltd., Wuhan, China) according to the manufacturer's instructions.

For Aβ-related stress experiments, human amyloid β peptide 1–42 ($A\beta_{1-42}$; P9001; Beyotime Biotechnology, Shanghai, China) was dissolved in dimethyl sulfoxide (DMSO) and prepared as oligomeric $A\beta_{1-42}$ before use. Oligomeric $A\beta_{1-42}$ was applied at a final concentration of 20 μM. HT22 cells were treated for 48 h, whereas primary neurons were treated for 24 h before downstream analyses. Control groups received the corresponding DMSO-containing vehicle treatment under the same conditions.

Western blotting

Western blotting was performed as previously described [32, 33] with minor modifications. Cells were lysed in RIPA lysis buffer (R0010; Beijing Solarbio Science & Technology Co., Ltd., Beijing, China) supplemented with protease and phosphatase inhibitors. Hippocampal tissues were homogenized on ice in lysis buffer at a ratio of 1:10 (*w*/*v*), followed by centrifugation. Supernatants were collected and protein concentrations were determined using a Pierce BCA Protein Assay Kit (23227; Thermo Fisher Scientific, Waltham, MA).

Equal amounts of protein were separated by 8% or 10% SDS-PAGE, depending on the molecular weight of the target protein, and transferred to PVDF membranes using the wet transfer method. Membranes were blocked with 5% non-fat milk and incubated with primary antibodies (Table S1) overnight at 4 °C. After washing, membranes were incubated with HRP-conjugated secondary antibodies (RS0002; Immunoway Biotechnology, Suzhou, China) for 1 h at room temperature. Protein signals were visualized using a Tanon 5200 chemiluminescence imaging system (Tanon Science & Technology Co., Ltd., Shanghai, China) and quantified with ImageJ. Target protein intensity was normalized to β-actin.

Immunoprecipitation-mass spectrometry (IP-MS) and co-immunoprecipitation (Co-IP)

To identify STAT4-associated proteins, IP-MS was performed. SH-SY5Y cells were lysed in Pierce IP Lysis Buffer (87787; Thermo Fisher Scientific, Rockford, IL) supplemented with protease inhibitors, and the lysates were incubated with IP-grade anti-STAT4 antibody (A4523; ABclonal Technology Co., Ltd., Wuhan, China) under standard immunoprecipitation conditions. Immune complexes were captured using Protein A/G beads (88802; Thermo Fisher Scientific, Rockford, IL), washed extensively to reduce nonspecific binding, and subjected to on-bead enzymatic digestion. The resulting peptides were analyzed by liquid chromatography-tandem mass spectrometry (LC–MS/MS), and candidate interacting proteins were ranked by enrichment and spectral evidence.

For validation of selected interactions, Co-IP assays were performed using mouse hippocampal tissue lysates. Equal amounts of lysate were incubated with anti-STAT4 antibody (A4523; ABclonal Technology Co., Ltd., Wuhan, China) and Protein A/G beads. In a parallel group, lysates were incubated with DNase I (D7073; Beyotime Biotechnology, Shanghai, China) before immunoprecipitation, in order to assess the possible contribution of nucleic acid to the associated complexes. After immunoprecipitation, bound proteins were eluted and analyzed by western blotting for STAT4 and hnRNPK.

Immunofluorescence and immunohistochemistry

For histological analyses, mice were euthanized after behavioral testing, and brain tissues were collected and fixed in 4% paraformaldehyde at 4 °C for 24 h. Fixed brains were dehydrated through graded ethanol, cleared in xylene, and embedded in paraffin. Coronal brain sections containing the hippocampus were prepared at a thickness of 3 μm using a HistoCore BIOCUT manual rotary microtome (Leica Biosystems Nussloch GmbH, Nussloch, Germany). Sections were mounted on positively charged glass slides, dried, and stored until staining.

For paraffin-embedded brain sections, tissues were deparaffinized, rehydrated, and subjected to antigen retrieval. Sections were permeabilized with PBS containing 0.3% Triton X-100 and blocked with 5% BSA before incubation with primary antibodies overnight at 4 °C. The primary antibodies used for immunofluorescence and immunohistochemistry, including antibodies against Aβ/6E10, 4HNE, STAT4, NeuN, and hnRNPK, are listed in Table S1, together with their sources, catalog numbers, experimental applications, and representative figure panels.

For immunofluorescence staining, signals were detected using either fluorophore-conjugated secondary antibodies or a tyramide signal amplification (TSA)-based protocol. TSA-based staining was performed using a mouse/rabbit treble-fluorescence immunohistochemical kit (RS0035; Immunoway Biotechnology, Suzhou, China) according to the manufacturer's instructions. Sections were then counterstained with kit-supplied DAPI, mounted with kit-supplied antifade mounting medium, and subjected to fluorescence imaging. TSA-based staining was used for selected analyses, including 6E10 and 4HNE staining and multiplex colocalization analyses. For immunohistochemistry, sections were incubated with HRP-conjugated goat anti-mouse or anti-rabbit IgG (H+L) secondary antibodies (RS0001 and RS0002; Immunoway Biotechnology, Suzhou, Jiangsu, China), according to the host species of the primary antibodies. The signals were visualized using a DAB Horseradish Peroxidase Color Development Kit (P0203; Beyotime Biotechnology, Shanghai, China), and sections were counterstained with hematoxylin staining solution (C0107; Beyotime Biotechnology, Shanghai, China). Negative controls with omission of the primary antibody were included in each staining run.

Fluorescence imaging was used to assess STAT4 colocalization with NeuN in mouse brain and the subcellular localization of STAT4 and hnRNPK in HT22 cells. Images were acquired under identical settings across groups using a 3DHISTECH P250 FLASH digital slide scanner (3DHISTECH Ltd., Budapest, Hungary). Changes in STAT4 and hnRNPK localization after $A\beta_{1-42}$ treatment were evaluated on the basis of images obtained under matched acquisition conditions.

Flow cytometry

Annexin V/7-AAD apoptosis assay

Cell apoptosis was assessed using an Annexin V-PE/7-AAD Apoptosis Detection Kit (40310ES50; Yeasen Biotechnology Co., Ltd., Shanghai, China) according to the manufacturer's instructions. Briefly, cells were harvested,

washed twice with cold PBS, and resuspended in 1× binding buffer at a density of 1×10^6 cells/mL.

A total of 100 μL cell suspension was incubated with 5 μL Annexin V-PE and 10 μL 7-AAD for 15 min at room temperature in the dark. After staining, 400 μL 1× binding buffer was added, and samples were analyzed within 1 h using a BD LSRFortessa flow cytometer (BD Biosciences, San Jose, CA). At least 10,000 events were collected for each sample. Apoptotic populations were defined by standard quadrant gating based on Annexin V-PE and 7-AAD staining.

Cell-cycle analysis

Cell-cycle analysis was conducted using the Cell Cycle and Apoptosis Analysis Kit (C1052; Beyotime Biotechnology, Shanghai, China). Cells were fixed with 70% ethanol, washed, and incubated with RNase A and propidium iodide staining solution. DNA content was analyzed by flow cytometry, and the proportions of cells in G0/G1, S, and G2/M phases were calculated using standard analysis procedures.

CUT&Tag assay

CUT&Tag was performed in SH-SY5Y cells using the NovoNGS® CUT&Tag® 4.0 High-Sensitivity Kit (N259; Novoprotein Scientific Inc., Suzhou, China) according to the manufacturer's instructions. Briefly, cells were cross-linked with 1% formaldehyde and quenched with glycine, followed by immobilization on ConA-coated magnetic beads. Samples were incubated with anti-STAT4 antibody (13028–1-AP; Proteintech Group, Inc., Wuhan, China) overnight at 4 °C, washed, and then incubated with pAG-Tn5 transposase. Tagmentation was initiated by Mg^{2+} activation at 37 °C. After termination of the reaction and protein digestion, DNA fragments were purified and subjected to PCR amplification for library construction. Libraries were quality-checked using an Agilent 2100 Bioanalyzer (Agilent Technologies, Santa Clara, CA) and sequenced on an Illumina platform (Illumina, Inc., San Diego, CA) using paired-end reads.

RNA sequencing (RNA-seq)

Total RNA was extracted from SH-SY5Y cells with *STAT4* overexpression, knockdown, or corresponding controls. RNA integrity was confirmed (RIN > 7) before library preparation. Poly(A)+ mRNA was enriched using oligo(dT) beads, fragmented, and reverse-transcribed to generate cDNA. Second-strand synthesis, end repair, A-tailing, adapter ligation, and PCR amplification were performed using the Hieff NGS® Ultima Dual-mode mRNA Library Prep Kit (12309ES24; Yeasen Biotechnology Co., Ltd., Shanghai, China) according to the manufacturer's protocol. Libraries were quality-controlled and sequenced on an Illumina NovaSeq platform with 150-bp paired-end reads. Differential expression and downstream pathway analyses were performed using standard pipelines.

RNA immunoprecipitation sequencing (RIP-seq) and RIP-qPCR

RIP-seq was performed in HT22 cells with *Stat4* overexpression using the PureBinding® RNA Immunoprecipitation Kit (P0101; Guangzhou Geneseed Biotech Co., Ltd., Guangzhou, China). Cells were lysed in buffer containing protease and RNase inhibitors. The lysates were incubated with antibody-coupled Protein A/G beads (anti-hnRNPK or control IgG) at 4 °C. After washing, RNA was eluted, treated with DNase, and purified for library construction and sequencing. For validation, RIP-qPCR was performed using primers targeting *Creb1* and *Nras* transcripts. Enrichment was calculated relative to input and IgG controls. Three technical replicates were included for each sample.

Reactive oxygen species (ROS) staining

Intracellular ROS levels were measured using a Reactive Oxygen Species Assay Kit (50101ES01; Yeasen Biotechnology Co., Ltd., Shanghai, China) according to the manufacturer's instructions, with the kit-provided Rosup used as the positive control at a final concentration of 100 μM. Briefly, cells were incubated with 10 μM DCFH-DA in serum-free medium for 30 min at 37 °C in the dark. After washing to remove excess probe, fluorescence was detected using a fluorescence microscope (Carl Zeiss Microscopy GmbH, Jena, Germany).

EdU incorporation assay

Cell proliferation was assessed using an EdU incorporation assay (C0075S/C0075L; Beyotime Biotechnology, Shanghai, China). Cells were incubated with 10 μM EdU for 2 h, fixed with 4% paraformaldehyde, permeabilized with 0.3% Triton X-100, and subjected to Click reaction according to the manufacturer's instructions. Nuclei were counterstained with DAPI and imaged by fluorescence microscopy.

TUNEL staining

Apoptosis in brain sections was assessed using a TUNEL In Situ Apoptosis Kit (E-CK-A325; Elabscience Biotechnology Co., Ltd., Wuhan, China) according to the manufacturer's instructions. Paraffin-embedded brain sections with a thickness of 3 μm were deparaffinized, rehydrated, and treated with proteinase K, followed by incubation with the TUNEL reaction mixture containing TdT enzyme and fluorescent labeling solution at 37 °C in the dark. After DAPI counterstaining and mounting,

TUNEL-stained sections were scanned using a P250 FLASH digital slide scanner (3DHISTECH Ltd., Budapest, Hungary).

Golgi staining

Dendritic spine morphology was analyzed using the FD Rapid GolgiStain™ Kit (PK401; FD NeuroTechnologies, Inc., Columbia, MD) according to the manufacturer's instructions. Brain tissues were immersed in impregnation solution (Solution A/B) for 2 weeks in the dark, followed by incubation in Solution C. Coronal section (100 μm) were cut and stained, dehydrated, cleared, and mounted for imaging. Dendritic spine density was quantified in hippocampal neurons under blinded conditions.

Sholl analysis

Primary neurons were imaged under identical acquisition settings and traced using ImageJ with the Sholl Analysis plugin. Concentric circles were placed at 10-μm radial intervals extending from the center of the soma to a maximum radius of 100 μm, and the number of dendritic intersections at each radius was quantified. Sholl profiles were analyzed by mixed-effects analysis with radial distance as the repeated factor, and summary parameters including area under the curve and maximal intersection number were analyzed by two-way ANOVA with Tukey's multiple-comparison test.

ELISA

Soluble $A\beta_{1-42}$ levels in hippocampal tissues were measured using a mouse-specific ELISA kit (ml037956; Shanghai MLBIO Biotechnology Co., Ltd., Shanghai, China) according to the manufacturer's instructions. Absorbance was measured at 450 nm using a microplate reader (Thermo Fisher Scientific, Waltham, MA), and concentrations were calculated based on standard curves.

Statistical analysis

Statistical analyses were performed using R software (version 4.3.1). Data are presented as mean ± SEM unless otherwise indicated. Comparisons between two groups were analyzed using two-tailed unpaired Student's *t*-tests. Comparisons involving two independent variables were analyzed by two-way ANOVA followed by Tukey's multiple-comparison test. For time-course or repeated-measures datasets, including Sholl profiles and behavioral training curves, mixed-effects analysis or repeated-measures ANOVA was used as appropriate, followed by post-hoc multiple-comparison correction. The statistical tests, group sizes, and definitions of biological replicates are provided in the corresponding figure legends. A P value < 0.05 was considered statistically significant.

Results

STAT4 is reduced in AD neurons and enriched in neuronal populations

To identify neuronal factors consistently altered in AD, we integrated three independent human snRNA-seq datasets and examined the overlap of downregulated genes in neuronal populations. UMAP visualizations of the three datasets are shown in Fig. S1. This analysis identified STAT4 as a consistently downregulated candidate across the three datasets (Fig. 1a). Quantitative analyses across all three human snRNA-seq datasets showed that *STAT4* mRNA levels were lower in AD neurons than in control neurons (Fig. 1b).

We next examined the cell-type distribution of *STAT4* expression. In both the human snRNA-seq dataset GSE222007 and the mouse scRNA-seq dataset GSE261596 generated from 3×Tg-AD and corresponding WT mice, *STAT4* expression was enriched in neuronal populations relative to other major cell types (Fig. 1c, d). In line with these transcriptomic observations, immunofluorescence analyses in the hippocampi of 3×Tg, 5×FAD, and WT mice showed colocalization of STAT4

(See figure on next page.)

Fig. 1 STAT4 is reduced in AD neurons and enriched in neuronal populations. **a** Venn diagram showing overlapping downregulated genes in neuronal populations across three independent snRNA-seq datasets (GSE222007, GSE188545, and GSE157827), identifying *STAT4* as a shared candidate. **b** *STAT4* mRNA levels comparison between AD and control neurons across the three human snRNA-seq datasets. **c** Violin plots showing cell type-stratified *STAT4* expression in the snRNA-seq dataset GSE222007. **d** Violin plots showing cell type-stratified *Stat4* expression in the mouse scRNA-seq dataset GSE261596. **e** Immunofluorescence analysis showing colocalization of STAT4 with NeuN in the hippocampus of 3×Tg, 5xFAD, and WT mice. **f**, **g** Representative western blots and quantification of STAT4 protein levels in HT22 cells treated with oligomeric $A\beta_{1-42}$ (20 μM, 48 h). **h**, **i** Representative western blots and quantification of STAT4 protein levels in mouse primary neurons treated with oligomeric $A\beta_{1-42}$ (20 μM, 24 h). **j**–**m** Representative western blots and quantification of STAT4 protein levels in the cortex and hippocampus of 3×Tg and WT mice at 3, 6, and 9 months of age. Data are presented as mean ± SEM. Statistical significance was determined by two-tailed unpaired Student's *t*-test, one-way ANOVA, or two-way ANOVA followed by appropriate post hoc tests, as appropriate. *$P < 0.05$, **$P < 0.01$, ***$P < 0.001$, ****$P < 0.0001$. Human snRNA-seq datasets are used in panels **a**–**c**; a mouse scRNA-seq dataset is used in panel **d**; mouse hippocampal tissues, HT22 cells, and mouse primary neurons are used in panels **e**–**m**

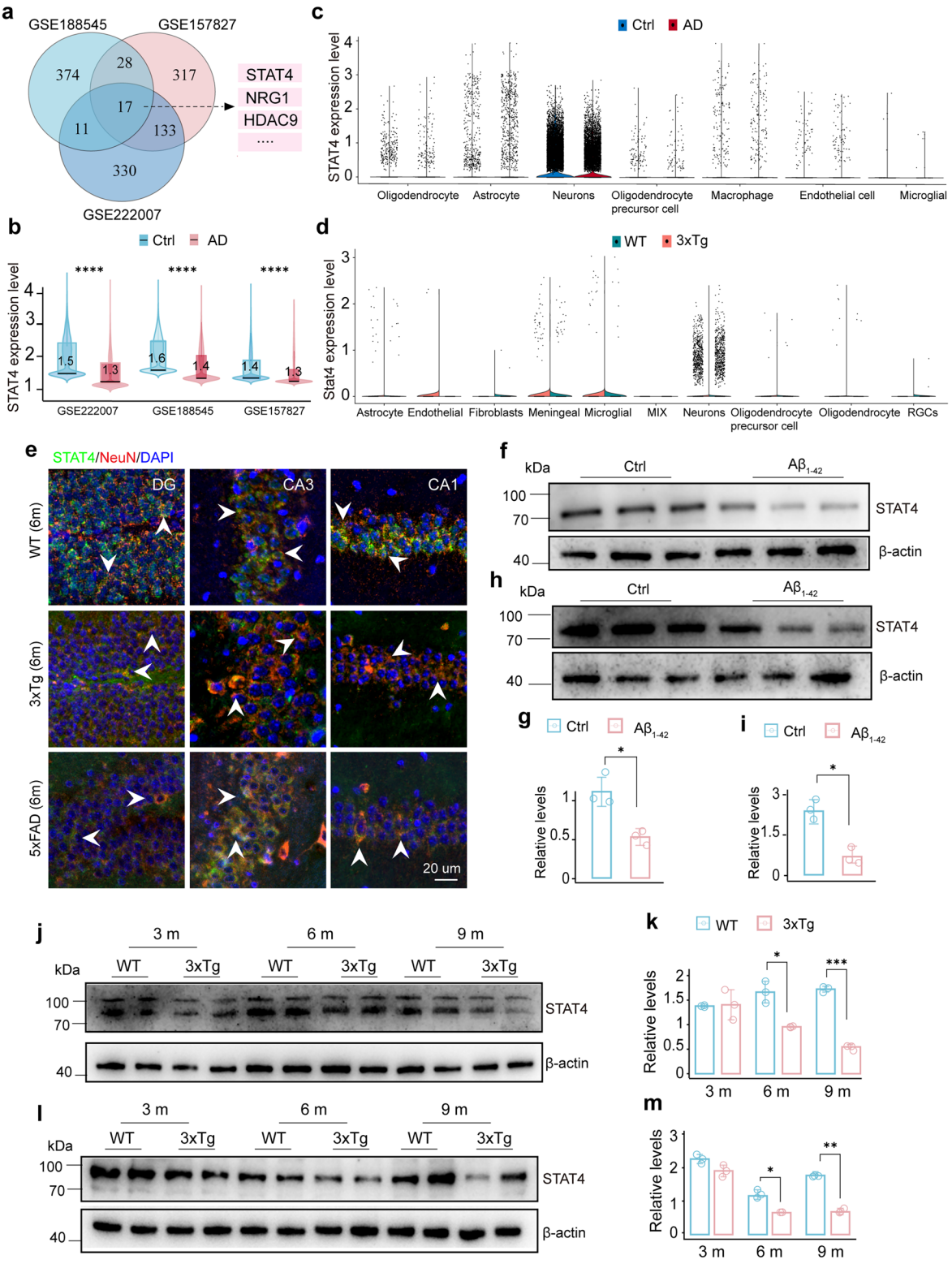

Fig. 1 (See legend on previous page.)

with the neuronal marker NeuN (Fig. 1e), supporting its neuronal association in vivo.

To determine whether AD-related stress affects STAT4 expression, we treated neuronal cells with oligomeric $A\beta_{1-42}$. Western blot analyses showed reduced STAT4 protein levels in mouse HT22 neuronal cells after Aβ exposure (Fig. 1f, g). A similar reduction was observed in mouse primary neurons derived from WT fetal mice treated with oligomeric $A\beta_{1-42}$ (Fig. 1h, i). In vivo, western blot analyses of cortical and hippocampal tissues from 3×Tg and WT mice at 3, 6, and 9 months of age showed that STAT4 protein levels were significantly reduced in 3×Tg mice from 6 months onward (Fig. 1j–m). This temporal pattern informed the selection of 5-month-old mice for subsequent in vivo experiments.

Taken together, these findings identify STAT4 as a neuron-associated factor reduced in AD-related human datasets, Aβ-treated neuronal cells, and AD mouse brains.

STAT4 is required for neuronal integrity and synaptic maintenance

Given the neuronal enrichment of STAT4 and its reduction in AD-related settings, we next asked whether STAT4 is functionally required for neuronal maintenance under basal conditions. In the human GTEx BA9 cortex and hippocampus, STAT4 expression was positively correlated with the neuronal and synaptic markers DLG4, SYP, and RBFOX3 (Fig. 2a, b), suggesting an association between STAT4 abundance and neuronal and synaptic status in human brain tissue.

To test this experimentally, we knocked down *Stat4* in HT22 cells. Flow-cytometric analysis showed a reduction in the S-phase population following STAT4 knockdown (Fig. 2c, d), suggesting an altered cell-state response. In parallel, western blot analyses demonstrated decreased protein levels of PSD95, SYP, and NeuN (Fig. 2i, j).

Similar results were obtained in primary mouse neurons, in which *Stat4* knockdown also reduced PSD95, SYP, and NeuN protein levels (Fig. 2e, f). Morphological analysis further showed that STAT4 depletion impaired neuronal structure. Sholl analysis demonstrated reduced dendritic complexity in primary neurons following *Stat4* knockdown, and this structural impairment became more pronounced under oligomeric $A\beta_{1-42}$ treatment (Fig. 2g, h).

Together, these data indicate that STAT4 is required for neuronal integrity and synaptic maintenance, and that loss of STAT4 impairs synaptic protein expression and dendritic structure, with further exacerbation under AD-related stress.

STAT4-bound and STAT4-responsive genes converge on neuronal signaling and stress-associated regulatory programs

To explore the downstream regulatory architecture associated with STAT4, we performed Cut&Tag assay and RNA-seq in human SH-SY5Y cells. STAT4 Cut&Tag sequencing was performed to identify STAT4-bound genomic regions. KEGG pathway enrichment analysis of these STAT4-bound regions highlighted signaling pathways and neuron-associated pathways, including neuroactive ligand-receptor interaction, glutamatergic synapse, neurotrophin signaling pathway, axon guidance, and additional receptor-associated and intracellular signaling programs (Fig. S2a). In parallel, RNA-seq datasets were generated from SH-SY5Y cells under *STAT4* overexpression or knockdown conditions to identify STAT4-responsive transcriptional programs. KEGG pathway enrichment analyses of differentially expressed genes highlighted neuronal signaling, synaptic regulation, metabolic and stress-associated cell-state pathways, including neuroactive ligand-receptor interaction, glutamatergic synapse, synaptic vesicle cycle, oxidative phosphorylation, and PI3K/RAS/MAPK signaling programs (Fig. S2b, c).

We further integrated the STAT4 Cut&Tag and RNA-seq datasets to prioritize genes associated with STAT4-bound genomic regions that were also transcriptionally responsive to STAT4 perturbation. Enrichment analyses of these overlapping gene sets highlighted convergent regulatory programs related to neuronal communication,

(See figure on next page.)

Fig. 2 STAT4 is required for neuronal integrity and synaptic maintenance. **a**, **b** Correlation analyses between STAT4 and neuronal/synaptic markers (DLG4, SYP, RBFOX3) in GTEx BA9 cortex and hippocampus. **c**, **d** Flow cytometric analysis and quantification of cell-cycle distribution in HT22 cells following STAT4 knockdown. **e**, **f** Representative western blots and quantification of PSD95, SYP, and NeuN protein levels in mouse primary neurons after STAT4 knockdown. **g** Representative images of mouse primary neurons transduced with Ctrl or shSTAT4 and treated with vehicle or oligomeric $A\beta_{1-42}$ followed by Sholl analysis of dendritic complexity. **h** Sholl profiles showing the number of intersections at increasing radial distances from the soma in the indicated groups. **i**, **j** Representative western blots and quantification of PSD95, SYP, and NeuN protein levels in HT22 cells after STAT4 knockdown. Data are presented as mean ± SEM. Statistical significance for Sholl profiles was assessed by mixed-effects analysis with radial distance as the repeated factor, followed by Tukey's multiple-comparison test. Other comparisons were analyzed by two-tailed unpaired Student's *t*-test. $^{*}P < 0.05$, $^{**}P < 0.01$, $^{***}P < 0.001$; $^{\#}P < 0.05$, $^{\#\#}P < 0.01$, $^{\#\#\#}P < 0.001$. Human GTEx brain data are used in panels **a** and **b**; HT22 cells and mouse primary neurons are used in panels **c**–**j**

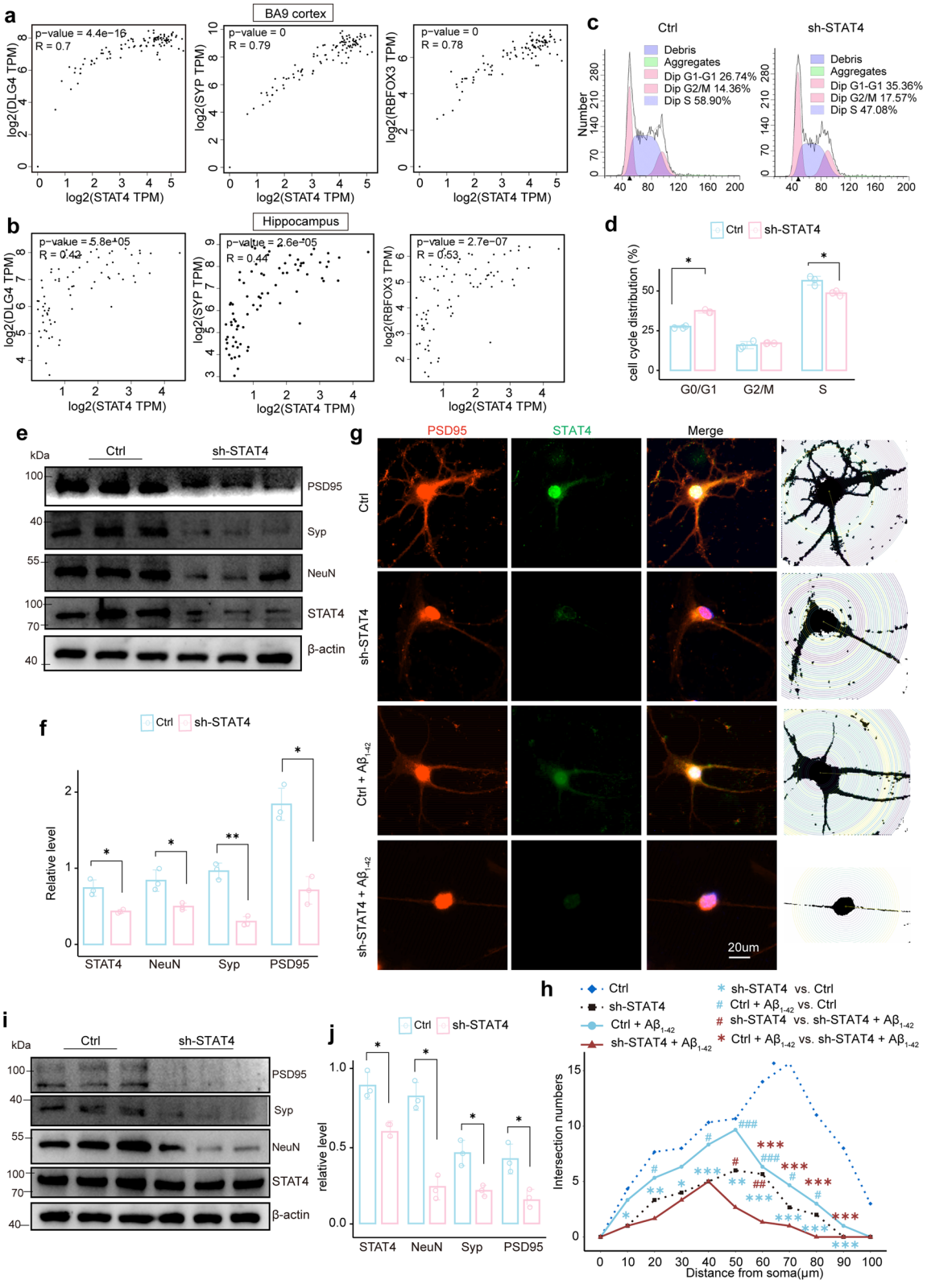

Fig. 2 (See legend on previous page.)

synaptic signaling, intracellular signal transduction, and stress-associated responses (Fig. 3a, b).

To extend this observation to human AD data, we performed WGCNA, a network-based approach used to identify modules of co-expressed genes and examine their relationships with genes or traits of interest, using the human AD dataset GSE203206. The scale-free topology fit index, mean connectivity, clustering dendrogram, and module assignment used for network construction are shown in Fig. S2d, e. Correlation heatmap analysis revealed coordinated relationships between *STAT4* and genes associated with the PI3K/RAS/MAPK pathway (Fig. 3c), and network visualization of the turquoise module further supported their co-expression structure (Fig. 3d).

In addition, in the human AD dataset GSE159699, *STAT4* mRNA levels were positively correlated with *CCND2* and *SOD1* expression (Fig. 3e, f). Because CCND2 is associated with cell-state regulation and SOD1 is involved in oxidative stress responses, these correlations support an association of STAT4 with transcriptional programs related to cell-state and stress-associated regulations in human AD data.

We then examined selected phosphorylation-related signaling readouts at the protein level in HT22 cells. STAT4 overexpression increased p-PI3K, p-AKT, p-MEK, and p-ERK levels, whereas its knockdown showed the opposite trend (Fig. 3g–i). To further assess phosphorylation-related changes relative to the total protein abundance, we calculated p-PI3K/PI3K, p-AKT/AKT, p-MEK/MEK, and p-ERK/ERK ratios, and found that these ratios were increased following *Stat4* overexpression and decreased following *Stat4* knockdown (Fig. 3j, k).

Taken together, the chromatin-binding, transcriptomic, integrative, co-expression, and biochemical analyses indicate that STAT4 is linked to coordinated intracellular signaling networks involving neuronal communication, stress-associated regulatory programs, and selected PI3K/AKT- and MAPK/ERK-related signaling outputs. These observations suggest that alterations of the downstream signaling balance may contribute to later stress-associated neuronal outcomes. Notably, several of these STAT4-associated signaling changes are linked to oxidative stress and apoptosis-related cellular responses, prompting further investigation into their functional consequences.

STAT4 overexpression produces time-dependent divergence in cellular outputs associated with stress responses

Because STAT4 was linked to signaling pathways involved in cell-state regulation, we next examined whether STAT4-associated signaling outputs lead to oxidative stress and apoptosis-related changes over time. We established a Tet-on inducible STAT4 overexpression system in HT22 cells. Under short-term induction for 48 h, STAT4 overexpression increased EdU incorporation (Fig. 4a, b), indicating an altered early cell-state response. At the same time point, Annexin V analysis did not show a statistically significant increase in apoptotic cells relative to the corresponding control group (Fig. 4c, d), suggesting that early STAT4 activation was not accompanied by an overt apoptotic phenotype.

By contrast, under sustained STAT4 overexpression for more than 72 h, the cellular profile shifted. Flow-cytometric analysis showed a reduction in the S-phase fraction (Fig. 4e, f), indicating impaired cell-cycle progression during sustained overexpression. In parallel, Annexin V staining showed increased apoptosis following sustained STAT4 overexpression (Fig. 4g, h), consistent with a transition toward a less favorable late-phase cellular state.

To further assess late-phase stress-related changes, we examined signaling readouts together with ROS staining. Western blot analysis showed that sustained STAT4 overexpression was associated with increases of p-AKT, p-ERK, CCND1, CCND2, p-p53 and cleaved caspase-9; these late-phase changes were attenuated by treatment with the ERK inhibitor PD0325901 (PDi, 50 nM) (Fig. 4i,

(See figure on next page.)

Fig. 3 STAT4-bound and STAT4-responsive genes converge on neuronal signaling and intracellular regulatory networks. **a**, **b** KEGG pathway enrichment analysis of overlapping genes identified by integrating STAT4 Cut&Tag-defined bound regions with RNA-seq datasets generated from SH-SY5Y cells under STAT4 overexpression (**a**) or STAT4 knockdown (**b**) conditions. **c** WGCNA correlation heatmap showing relationships between STAT4 and PI3K/RAS/MAPK-associated genes in the human AD dataset GSE203206. **d** Network visualization of the turquoise module highlighting co-expression relationships among STAT4-associated genes. **e**, **f** Correlation analyses of STAT4 with CCND2 (**e**) and SOD1 (**f**) mRNA levels in the human AD dataset GSE159699. **g** Representative western blots of p-PI3K, p-AKT, p-MEK, and p-ERK levels in HT22 cells following STAT4 overexpression or STAT4 knockdown. **h**, **i** Quantification of p-PI3K, p-AKT, p-MEK, and p-ERK levels following STAT4 overexpression (**h**) or STAT4 knockdown (**i**). **j**, **k** Quantification of p-PI3K/PI3K, p-AKT/AKT, p-MEK/MEK, and p-ERK/ERK ratios in HT22 cells following STAT4 overexpression (**j**) or STAT4 knockdown (**k**). Data are presented as mean ± SEM from three independent experiments. Statistical significance was determined by two-tailed unpaired Student's *t*-test. **P* < 0.05, ***P* < 0.01, ****P* < 0.001. SH-SY5Y cells are used for Cut&Tag/RNA-seq analyses in panels **a** and **b**; human AD transcriptomic datasets are used in panels **c**-**f**; HT22 cells are used for protein-level signaling analyses in panels **g**–**k**

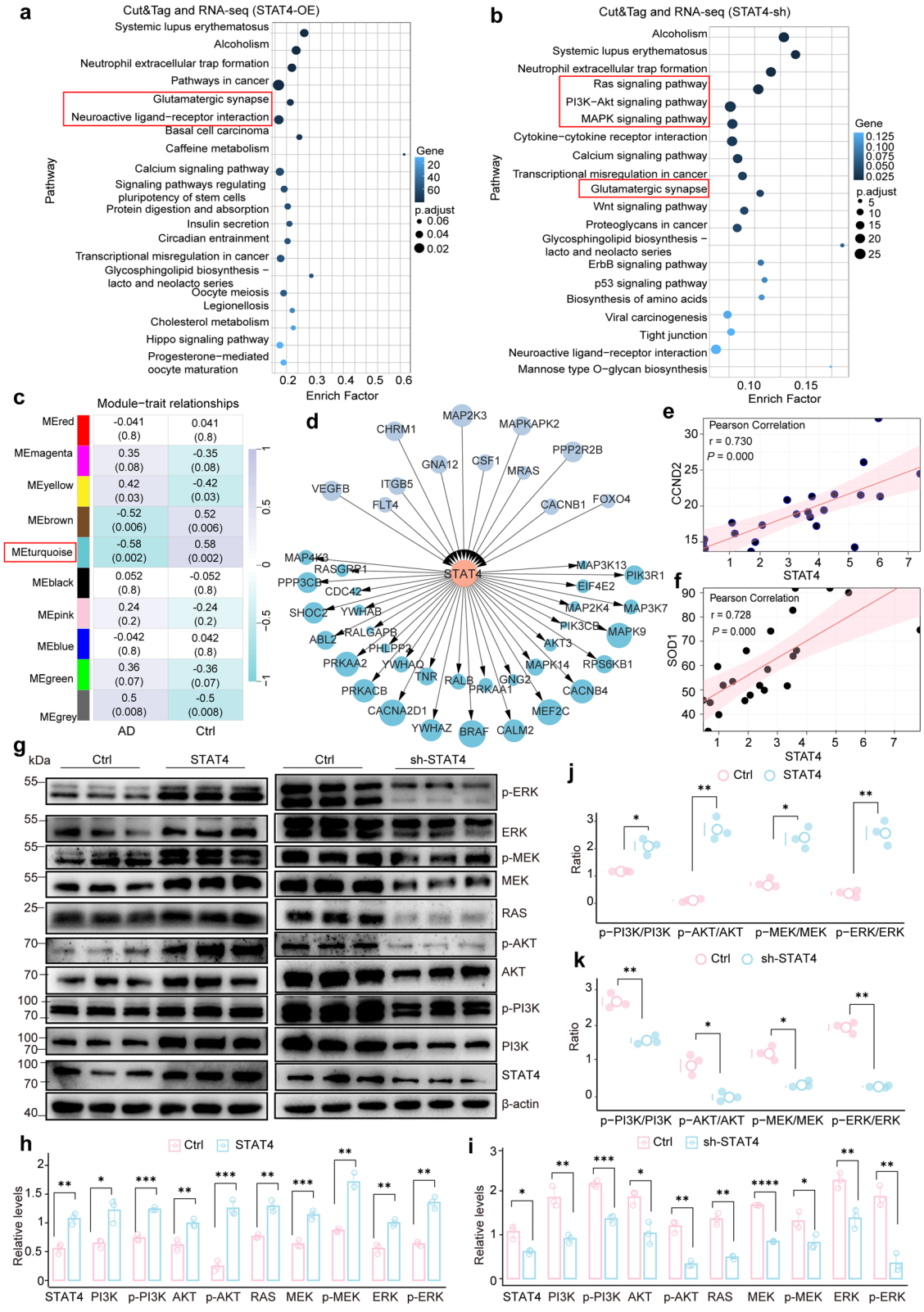

Fig. 3 (See legend on previous page.)

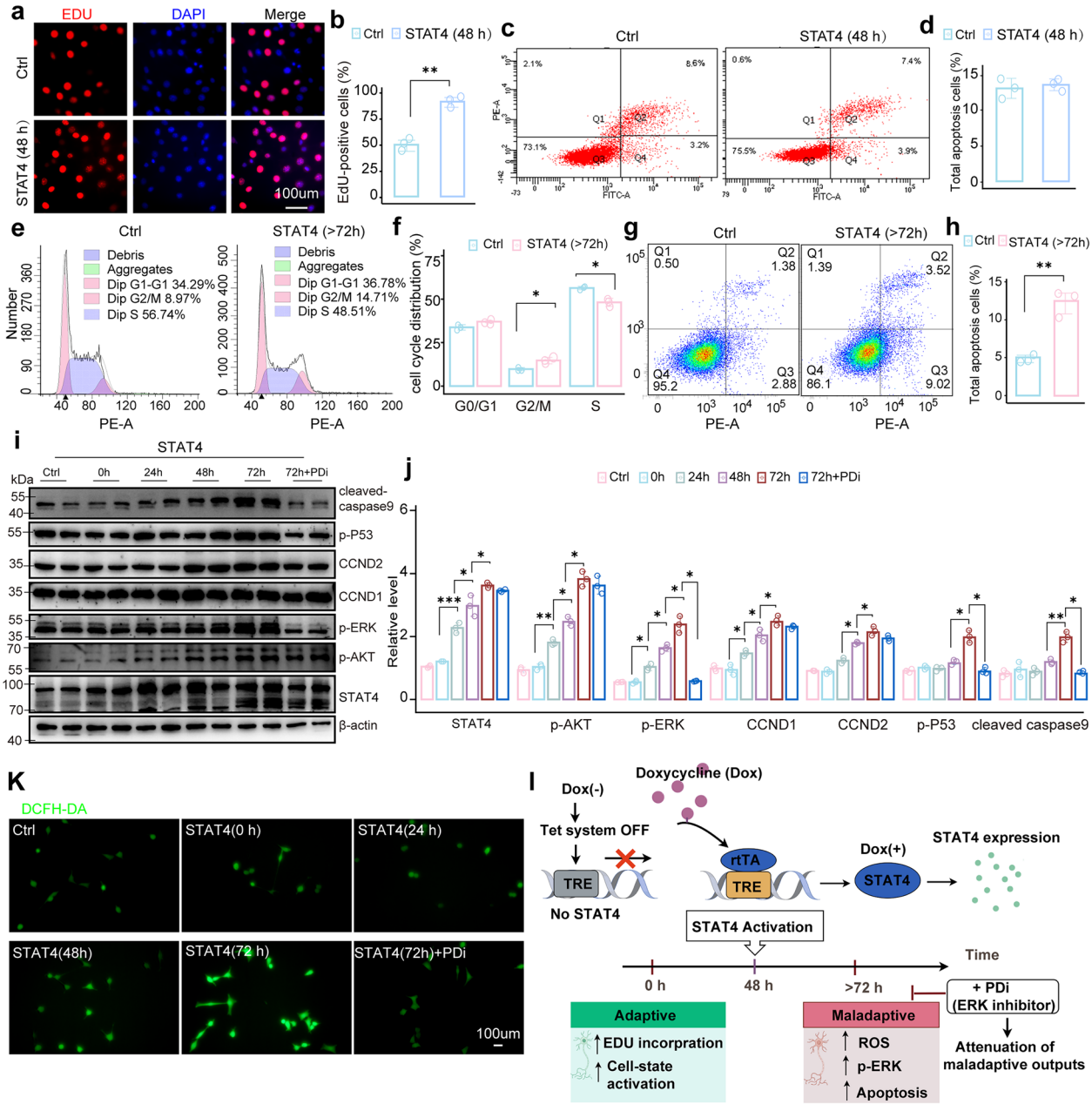

Fig. 4 STAT4 overexpression produces time-dependent divergence in cellular output in HT22 cells. **a**, **b** EdU incorporation assay and quantification in control and STAT4-overexpressing HT22 cells at 48 h. **c**, **d** Annexin V staining and quantification in control and STAT4-overexpressing HT22 cells at 48 h. **e**, **f** Cell-cycle analysis and quantification following sustained STAT4 overexpression (> 72 h). **g**, **h** Annexin V staining and quantification showing apoptosis following sustained STAT4 overexpression. **i**, **j** Representative western blots and quantification of p-AKT, p-ERK, CCND1, CCND2, p-p53, and cleaved caspase-9 in HT22 cells overexpressing STAT4 with or without ERK inhibitor treatment (PDi, 50 nM, 48 h). **k** Representative DCFH-DA staining showing ROS signal in HT22 cells overexpressing STAT4, with or without ERK inhibitor treatment (PDi, 50 nM, 48 h). **l** Schematic summary of time-dependent divergence in STAT4-associated outputs. Early STAT4 overexpression is associated with adaptive cellular features, whereas sustained overexpression is associated with oxidative stress- and apoptosis-related changes. Late-phase outputs are attenuated by ERK inhibition. Data are presented as mean ± SEM from three independent experiments. Statistical significance was determined by two-tailed unpaired Student's *t*-test or one-way ANOVA with Tukey's multiple-comparison test, as appropriate. **P* < 0.05, ***P* < 0.01, ****P* < 0.001

j). DCFH-DA staining further showed increased ROS signal in STAT4-overexpressing HT22 cells, which was reduced by PDi (Fig. 4k), providing visual evidence for enhanced oxidative stress during the late phase.

Taken together, these findings indicate that STAT4 overexpression produces time-dependent divergence in cellular output, with early induction associated with a comparatively adaptive cellular state and prolonged overexpression associated with oxidative stress- and apoptosis-related changes (Fig. 4l).

ERK inhibition attenuates STAT4-associated oxidative stress and apoptosis in vivo

We next examined whether ERK activity contributes to the STAT4-associated oxidative stress and apoptosis in vivo. To examine temporal dynamics and intervention effects, 5-month-old 3×Tg-AD and WT mice received hippocampal injection of AAV-hSyn-STAT4(K24K0126)-EGFP for STAT4 overexpression or vector control AAV-hSyn-EGFP. The mice were assessed at 4-week time point for early-stage effects. For the 8-week endpoint, ERK inhibition was introduced during weeks 4–8 after AAV injection by oral administration of PDi (10 mg/kg [28]) or vehicle. In parallel, WT groups were assessed at 4, 8, and 12 weeks to examine the function of STAT4 in a non-AD context.

In hippocampal sections, immunofluorescence analysis of the oxidative stress marker 4HNE showed that STAT4 overexpression was not associated with a comparable increase at 4 weeks, whereas a clear increase was observed at 8 weeks under sustained overexpression (Fig. 5a, b). This result was further supported by immunohistochemical staining of 4HNE in hippocampal tissues (Fig. 5e, f). Notably, the increased 4HNE signal in the 8-week STAT4 group was reduced by PDi (Fig. 5a, b, e, f), indicating that the late oxidative stress phenotype was sensitive to ERK inhibition.

To assess cell death in vivo, we performed TUNEL staining. In 3×Tg mice, the number of apoptotic cells was elevated after 8 weeks of STAT4 overexpression, but not at 4 weeks (Fig. 5i, j). This increase was attenuated by PDi treatment (Fig. 5i, j). Western blot analyses of hippocampal lysates further showed that p-p53 and cleaved caspase-9 were significantly increased at 8 weeks but not at 4 weeks, and both were reduced by PDi treatment (Fig. 5m, n), consistent with enhanced apoptosis-related signaling during sustained STAT4 overexpression.

We next examined tau-related changes. In 3×Tg mice, prolonged STAT4 overexpression was associated with significantly increased p-GSK3β (Tyr216) and phosphorylation of tau at Ser202/Thr205 and Ser396 at the 8-week time point compared to the earlier 4 weeks (Fig. 5m, n). These tau-associated changes at 8 weeks were attenuated by PDi treatment, indicating that the late pathological output associated with sustained STAT4 overexpression was at least partly ERK-sensitive.

In WT mice, comparable pathological changes did not emerge at the corresponding earlier time points. Instead, the trajectory was delayed, with oxidative stress-, apoptosis-, and tau-associated changes becoming detectable after 12 weeks of STAT4 overexpression, rather than at the 4- or 8-week time points (Fig. 5c, d, g, h, k, l, o, p). Taken together, these data show that prolonged STAT4 overexpression in vivo is accompanied by time-dependent increases in oxidative stress, apoptosis-related signaling, and tau-associated pathological changes, with earlier emergence in 3×Tg mice and delayed emergence in WT mice. In 3×Tg mice, these late-phase readouts were attenuated by ERK inhibition.

STAT4-associated beneficial outputs are preserved despite ERK inhibition

Because ERK inhibition attenuated the pathological outputs associated with sustained STAT4 overexpression, we next examined whether ERK blockade also affected other STAT4-associated phenotypes in vivo. In 3×Tg mice, STAT4 overexpression was associated with reduced Aβ plaque burden, as assessed by 6E10 immunostaining and immunohistochemistry (Fig. 6a, b, d, e), and with lower levels of soluble $A\beta_{1-42}$ measured by ELISA (Fig. 6g). These reductions were detectable at the assessed endpoint and remained evident in the 8-week STAT4 + PDi group (Fig. 6a, b, d, e, g), indicating that the Aβ-lowering effect associated with STAT4 overexpression was retained despite ERK inhibition. As expected, WT mice showed minimal Aβ burden across groups (Fig. 6c, f, h).

(See figure on next page.)

Fig. 5 Late pathological changes associated with STAT4 overexpression reflect ERK-biased maladaptive signaling in vivo. **a**–**d** Immunofluorescence images and quantification of 4HNE staining in hippocampal sections from 3×Tg-AD and WT mice across the indicated time points following STAT4 overexpression, with or without PDi treatment where indicated. **e**–**h** Immunohistochemical staining and quantification of 4HNE in hippocampal tissues from the indicated groups. **i**–**l** TUNEL staining and quantification of apoptotic cells in hippocampal sections from the indicated groups. **m**–**p** Representative western blots and quantification of apoptosis- and tau-related markers, including p-p53, cleaved caspase-9, p-GSK3β (Tyr216), and phosphorylated tau (Ser202/Thr205 and Ser396), in hippocampal lysates from the indicated groups. Data are presented as mean ± SEM. Statistical significance was determined by two-way ANOVA with Tukey's multiple-comparison test. *$P < 0.05$, **$P < 0.01$, ***$P < 0.001$

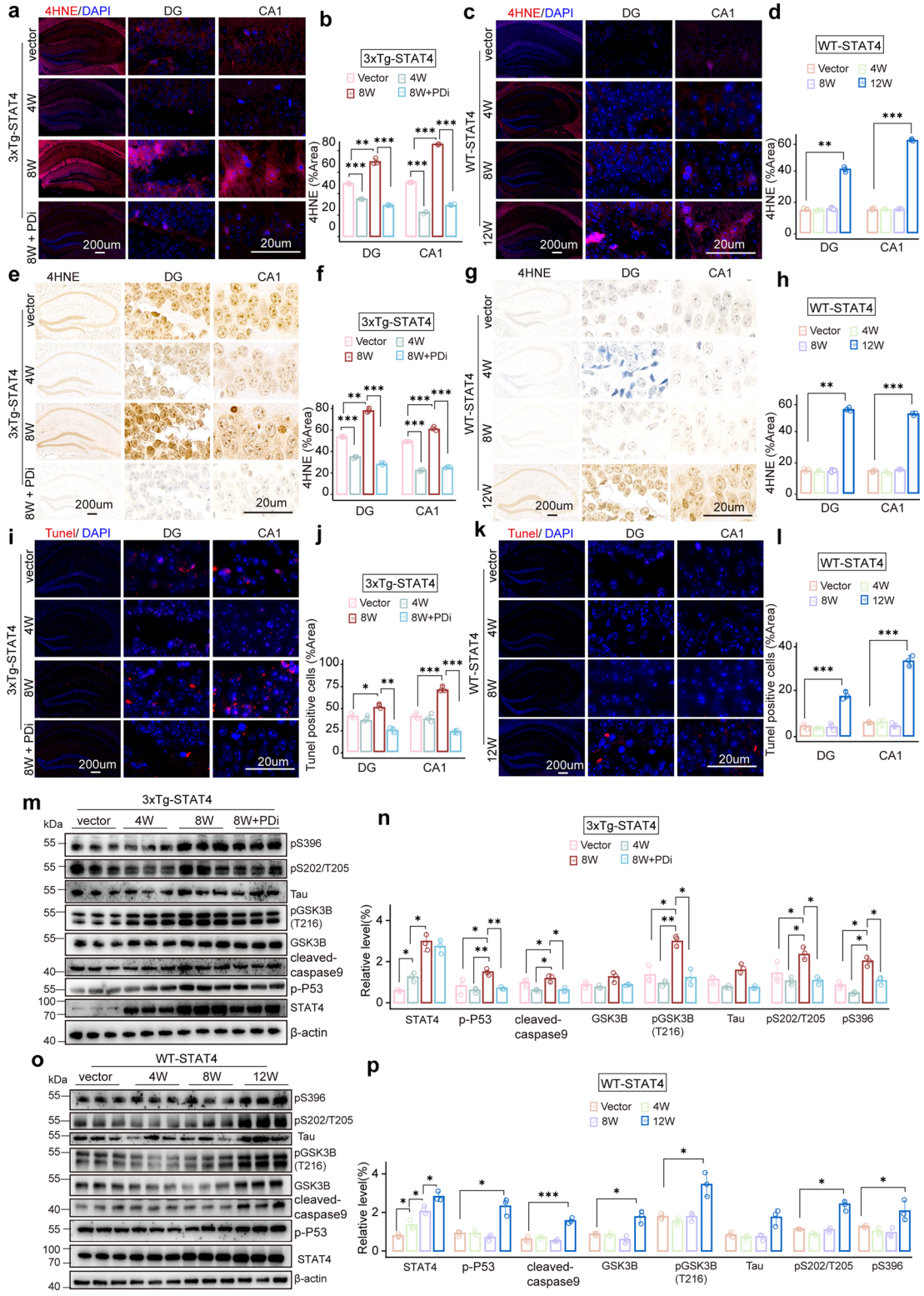

Fig. 5 (See legend on previous page.)

We next assessed structural and molecular readouts related to synaptic integrity. Golgi staining showed that the dendritic spine density in hippocampal neurons was increased in STAT4-overexpressing mice, and this increase remained detectable under combined STAT4 + PDi treatment (Fig. 6i, j). Consistently, western blot analyses of hippocampal lysates from 3×Tg mice showed that the levels of SYP, PSD95, and NeuN remained elevated in the 8-week STAT4 + PDi group (Fig. 6m, n).

Pathway activity was further evaluated by quantifying p-AKT/AKT and p-ERK/ERK ratios in the same hippocampal lysates. In 3×Tg mice, STAT4 overexpression increased both p-AKT/AKT and p-ERK/ERK ratios at the 4-week and 8-week time points compared with vector controls (Fig. 6o). Notably, at the 8-week endpoint, PDi treatment significantly reduced the STAT4-associated increase in p-ERK/ERK, whereas p-AKT/AKT was not significantly different compared to the 8-week STAT4 group (Fig. 6o). These results indicate that ERK inhibition effectively constrained ERK pathway activation while leaving STAT4-associated AKT signaling largely preserved. Importantly, the Aβ-lowering effect and the elevation of synaptic and neuronal markers remained detectable in the STAT4 + PDi group, indicating that these STAT4-associated beneficial outputs were not abolished by ERK inhibition (Fig. 6a–j, m–o). CCND1 and CCND2 were examined as additional STAT4-associated signaling or cell-state-related readouts but were not interpreted as direct markers of synaptic benefit (Fig. 6m, n).

Similar preservation of synaptic and neuronal markers was observed in WT mice, including at the 12-week time point (Fig. 6k, l, p, q). The p-AKT/AKT ratio was increased relative to vector controls at 4, 8, and 12 weeks following STAT4 overexpression. The p-AKT/AKT ratio increased progressively following STAT4 overexpression, with significant increases at 4 weeks compared to vector control, at 8 weeks compared to 4 weeks, and at 12 weeks compared to 8 weeks (Fig. 6r). In parallel, p-ERK/ERK was significantly increased at 4, 8, and 12 weeks compared with vector controls and showed a sustained increase with time in WT mice (Fig. 6r). These findings indicate that STAT4-associated AKT and ERK signaling activation also occurs in WT mice, whereas the emergence of overt pathological outputs is delayed compared with 3×Tg mice.

To further examine whether the sequencing and network data contained information relevant to the divergent in vivo outputs, we re-examined the integrated STAT4 Cut&Tag/RNA-seq analyses and extracted STAT4-centered nodes from the STAT4-related WGCNA turquoise module. In the integrated Cut&Tag/RNA-seq analyses, STAT4-bound and STAT4-responsive genes were enriched in neuronal and synaptic signaling pathways, including glutamatergic synapse and neuroactive ligand–receptor interaction, as well as intracellular signaling pathways, including PI3K-AKT, RAS/MAPK, and p53 signaling. Extraction of the WGCNA turquoise module identified STAT4-connected co-expression nodes related to amyloid biology, including APP and SORL1; tau-associated kinase/phosphatase regulation, including GSK3B, CDK5, MARK1, and PPP2CA; synaptic function, including SYP, GRIN2A, GRIN2B, and HOMER1; and oxidative stress, including SOD1. These results are summarized in Table S4. The WGCNA-derived relationships represent network-level associations rather than evidence of direct causal regulation.

Together, these findings indicate that selected STAT4-associated beneficial outputs, including reduced Aβ burden and improved synaptic and neuronal readouts, remain detectable when ERK activation is pharmacologically constrained. The selective reduction of p-ERK/ERK, but not p-AKT/AKT, by PDi in 3×Tg mice further supports differential sensitivity of STAT4 downstream outputs to ERK modulation.

Behavioral outcomes reflect the context-dependent divergence of STAT4-associated signaling

We next asked whether the molecular and histological divergence associated with STAT4 signaling was reflected at the behavioral level. Using the same in vivo treatment paradigm, we performed behavioral testing using MWM

(See figure on next page.)

Fig. 6 Beneficial STAT4-associated outputs are preserved despite ERK inhibition. **a**–**f** Representative immunofluorescence and immunohistochemistry images, with quantification, of Aβ plaque load (6E10) in hippocampal sections from 3×Tg-AD and WT mice across the indicated time points. **g**, **h** ELISA quantification of soluble $A\beta_{1-42}$ levels in brain homogenates from 3×Tg-AD and WT mice. **i**–**l** Representative Golgi staining images and quantification of dendritic spine density in hippocampal neurons. Scale bar, 10 μm. **m**, **n** Representative western blots and quantification of synaptic and neuronal markers (SYP, PSD95, NeuN), signaling readouts (p-AKT, total AKT, p-ERK, total ERK), and cell-state-associated proteins (CCND1, CCND2) in 3×Tg-AD mice. **o** Quantification of p-AKT/AKT and p-ERK/ERK ratios in hippocampal lysates from 3×Tg-AD mice across the indicated treatment groups and time points. **p**, **q** Representative western blots and quantification of corresponding markers and signaling readouts in WT mice across time points. **r** Quantification of p-AKT/AKT and p-ERK/ERK ratios in hippocampal lysates from WT mice across the indicated time points. Data are presented as mean ± SEM. Statistical significance was determined by one-way or two-way ANOVA followed by Tukey's multiple-comparison test, as appropriate. *$P < 0.05$, **$P < 0.01$, ***$P < 0.001$

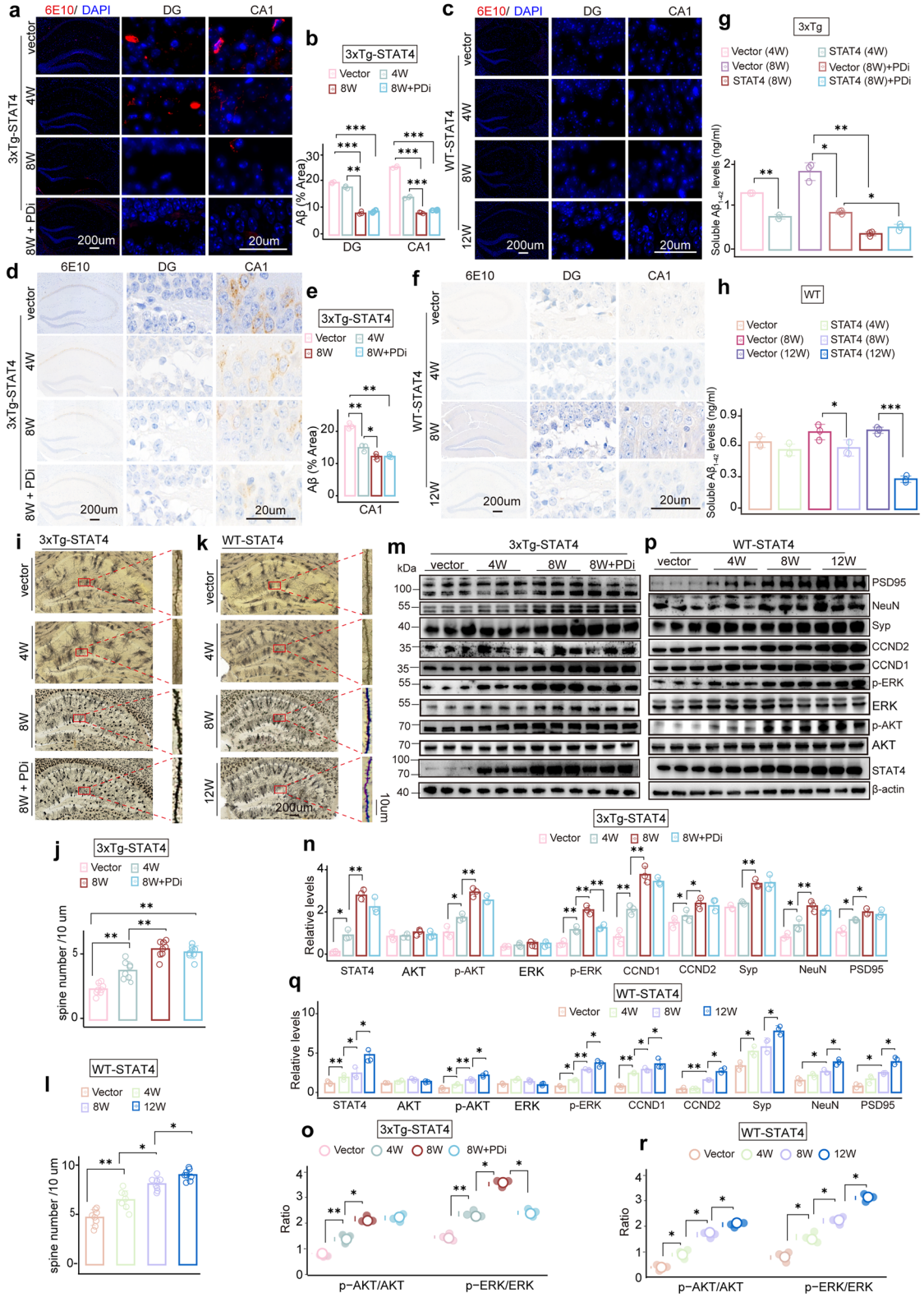

Fig. 6 (See legend on previous page.)

and NOR (Fig. 7a). Immunofluorescence analysis confirmed successful hippocampal overexpression of STAT4 across groups (Fig. 7b).

In the MWM assay, swimming traces illustrate spatial search patterns in different groups (Fig. 7c). During the training phase, escape latency differed across groups, with STAT4 overexpression associated with improved spatial learning at the early time point, followed by a relative reduction in performance under sustained overexpression. In the STAT4 + PDi group, this late-phase reduction was attenuated, and performance remained improved compared to the STAT4 group at 8 weeks (Fig. 7d). In 3×Tg mice, the vector-treated animals receiving PDi also showed a modest but statistically significant reduction in escape latency compared to the corresponding vehicle-treated group. In WT mice, the temporal pattern differed from that observed in 3×Tg mice, with no comparable early decline at 8 weeks and a delayed trajectory extending to 12 weeks (Fig. 7e). Notably, although the behavioral performance in the WT STAT4 (12W) group remained improved compared to the corresponding vector group, the difference did not reach statistical significance.

We next examined NOR performance (Fig. 7f). In the AD context, the vector-treated 3×Tg mice receiving ERK inhibition (vector + PDi) showed a trend toward increased novel object preference relative to the corresponding vehicle-treated control group, but this difference did not reach statistical significance (Fig. 7g, h). STAT4 overexpression was also associated with improved behavioral performance at the 4-week time point compared to control groups. However, under sustained overexpression (8 weeks), this improvement was reduced, although the novel object preference was still significantly higher than the corresponding vector-treated group. In the 8-week STAT4 + PDi group, novel object preference was higher than that in the STAT4 + vehicle group and remained significantly increased compared with the corresponding vector + PDi control group. In WT mice, the STAT4 (12W) group also showed an increase in novel object preference compared to the vector (12W) group, but this difference did not reach statistical significance. Thus, the NOR results support a time-dependent change in behavioral output in the AD context, while the behavioral effects in WT mice are weaker or delayed over the time window examined here.

The behavioral findings were integrated with the broader in vivo time-course pattern (Fig. 7i). In 3×Tg mice, the behavioral trajectory associated with sustained STAT4 overexpression shifted earlier toward a less favorable late-phase state, whereas in WT mice the corresponding change was delayed and less pronounced. This summary is consistent with the pathological and molecular data, supporting a genotype-dependent temporal divergence in STAT4-associated outputs in vivo.

Taken together, the behavioral data are consistent with a context-dependent divergence of STAT4-associated signaling in vivo. In the AD setting, sustained STAT4 overexpression produced measurable benefits compared to the control conditions, but the magnitude of improvement was reduced at later stages, whereas ERK inhibition produced a more favorable late-phase behavioral trajectory.

hnRNPK associates with STAT4 and may contribute to the coordinated signaling output

To further explore how STAT4 may coordinate divergent signaling outputs, we searched for candidate interacting proteins using IP-MS in SH-SY5Y cell lysates. Integrated spectral analyses identified hnRNPK and PCM1 as major candidate proteins associated with STAT4 (Fig. 8a, b). Given the RNA-binding capacity and the dual nucleocytoplasmic localization of hnRNPK, we selected it for further mechanistic analysis.

The interaction between STAT4 and hnRNPK was then examined in vivo and in cultured cells. Co-immunoprecipitation assays using hippocampal tissues from 3×Tg mice confirmed the association between STAT4 and hnRNPK, and DNase I treatment altered this interaction pattern (Fig. 8c), suggesting the possible involvement of nucleic acid-associated complexes. In the human AD dataset GSE203206, mRNA levels of STAT4 and hnRNPK were positively correlated (Fig. 8d). In HT22 cells, immunofluorescence analyses further showed subcellular colocalization of STAT4 and hnRNPK, which changed after $A\beta_{1-42}$ treatment (Fig. 8e, f). Under Aβ stress, nuclear

(See figure on next page.)

Fig. 7 Behavioral outcomes in 3×Tg-AD and WT mice reflect the context-dependent divergence of STAT4-associated signaling in vivo. **a** Experimental timeline of AAV-mediated STAT4 overexpression, ERK inhibition, and behavioral testing. **b** Representative immunofluorescence images confirming hippocampal STAT4 overexpression. Scale bars, 200 μm. **c** Representative swimming traces in the Morris water maze (MWM) probe trial. **d**, **e** Escape latency during MWM training in 3×Tg and WT mice under the indicated experimental conditions. **f** Schematic illustration of the novel object recognition (NOR) test procedure. **g**, **h** Quantification of novel object preference of 3×Tg and WT mice across indicated time points and treatment conditions. **i** Schematic summary of genotype-dependent temporal divergence in STAT4-associated outputs in vivo. Data are presented as mean ± SEM. NOR data were analyzed by two-way ANOVA with Tukey's multiple-comparison test, whereas MWM training data were analyzed using a mixed-effects model. Sample sizes were $n = 8–10$ mice per group. $^{*}P < 0.05$, $^{**}P < 0.01$, $^{***}P < 0.001$

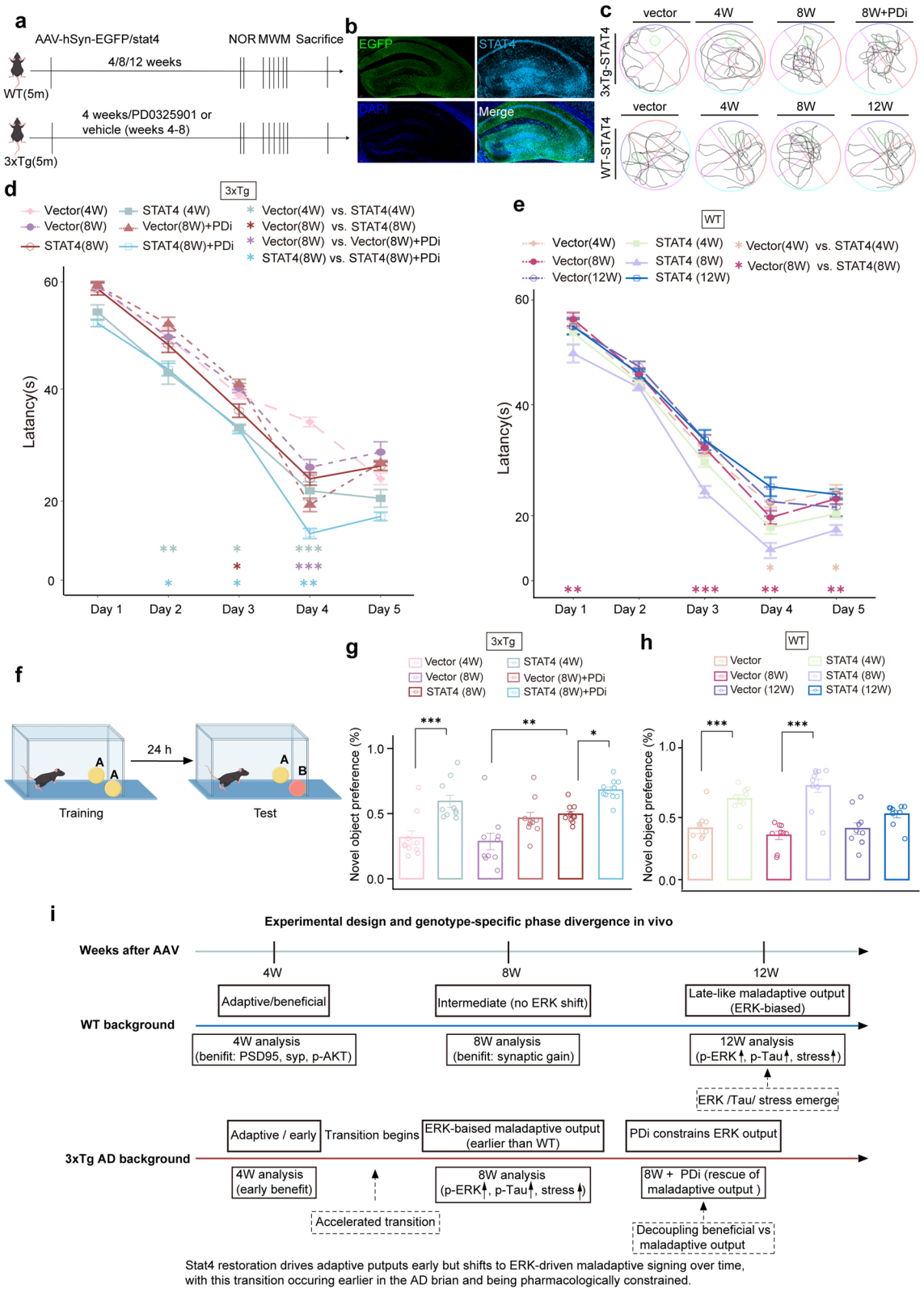

Fig. 7 (See legend on previous page.)

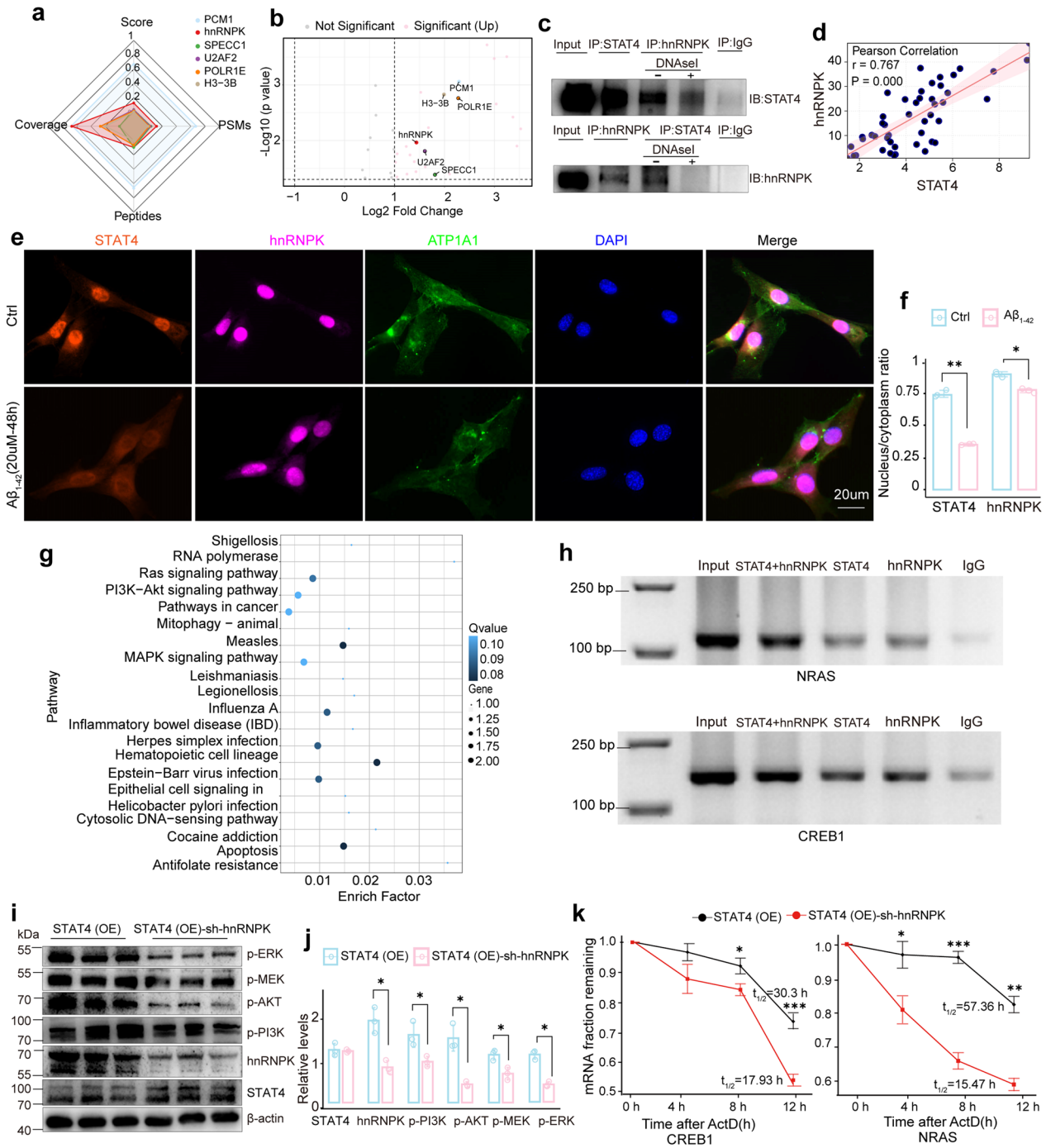

Fig. 8 hnRNPK associates with STAT4 and may contribute to coordinated signaling output. **a** Radar chart showing the top candidate STAT4-interacting proteins identified by IP-MS in SH-SY5Y cell lysates, ranked according to integrated spectral parameters including score, sequence coverage, unique peptides, and peptide-spectrum matches (PSMs). **b** Volcano plot of the IP-MS dataset showing proteins enriched in STAT4-associated complexes. **c** Co-immunoprecipitation analysis showing interaction between STAT4 and hnRNPK in mouse hippocampal lysates, with or without DNase I treatment. **d** Correlation of STAT4 and hnRNPK mRNA expression in the human AD dataset GSE203206. **e**, **f** Immunofluorescence images showing subcellular localization and colocalization of STAT4 and hnRNPK in HT22 cells under control and $A\beta_{1-42}$ treatment conditions. **g** Pathway enrichment analysis of hnRNPK-associated transcripts identified by RIP-seq in HT22 cells. **h** Agarose gel electrophoresis of RIP-qPCR products showing enrichment of CREB1 and NRAS transcripts in hnRNPK-associated complexes in HT22 cells. **i**, **j** Representative western blots and quantification of p-PI3K, p-AKT, p-MEK, and p-ERK levels in HT22 cells overexpressing STAT4 with or without hnRNPK knockdown. **k** mRNA stability analysis of CREB1 and NRAS using actinomycin D chase assays in STAT4-overexpressing HT22 cells with or without hnRNPK knockdown. Data are presented as mean ± SEM. Statistical significance was determined by two-tailed unpaired Student's *t*-test or one-way ANOVA with Tukey's multiple-comparison test, as appropriate. **P* < 0.05, ***P* < 0.01, ****P* < 0.001

localization of both proteins was reduced, while STAT4 showed more prominent cytoplasmic retention.

To explore the functional relevance of hnRNPK, we analyzed RIP-seq data generated from STAT4-overexpressing HT22 cells and found enrichment of hnRNPK-associated transcripts in PI3K/RAS/MAPK-related pathways (Fig. 8g). RIP-qPCR assays further supported enrichment of CREB1 and NRAS transcripts in hnRNPK-associated complexes (Fig. 8h). Functionally, hnRNPK knockdown attenuated the increase in p-PI3K, p-AKT, p-MEK, and p-ERK induced by STAT4 overexpression (Fig. 8i, j). Moreover, in actinomycin D chase experiments, hnRNPK knockdown shortened the half-lives of *Creb1* and *Nras* mRNAs in STAT4-overexpressing HT22 cells (Fig. 8k).

Together, these data suggest that hnRNPK associates with STAT4 and may contribute to the coordinated regulation of signaling output at both the protein and the transcript levels.

Discussion

In the present study, we identified STAT4 as a neuronal regulator whose sustained activation is associated with stress-associated cellular responses and apoptosis-related changes. These findings position STAT4 not only as a regulator of neuronal homeostasis but also as a factor that can drive stress-associated cellular responses under specific conditions. By integrating transcriptomic analyses with cellular and in vivo experiments, we show that STAT4 supports neuronal and synaptic homeostasis while engaging both PI3K/AKT and MAPK/ERK signaling pathways. In the context of AD, however, this dual-output signaling framework becomes progressively imbalanced, resulting in ERK-biased maladaptive changes despite retention of selected beneficial downstream effects.

A notable finding of the present study is that STAT4 appears to support neuronal integrity and synaptic homeostasis under basal conditions. Transcriptomic correlations in human brain datasets, together with functional assays in neuronal systems, consistently link STAT4 to neuronal and synaptic integrity. These observations extend the current understanding of STAT4 beyond its established role in immune regulation. Notably, accumulating evidence suggests that immune-associated transcriptional regulators can also participate in neuronal homeostasis and neurodegenerative processes [34–37], although this aspect remains incompletely defined.

Our data further indicate that STAT4-associated outputs are not fixed, but evolve over time. In inducible neuronal systems, short-term STAT4 restoration was associated with adaptive features, whereas sustained STAT4 expression was accompanied by oxidative stress- and apoptosis-related signaling. This time-dependent divergence was recapitulated in vivo, where prolonged STAT4 elevation in 3×Tg mice was associated with oxidative stress, neuronal injury, and tau-related changes. The time points selected in this study were intended to capture both early and sustained phases of STAT4 elevation, guided by the temporal pattern of endogenous STAT4 reduction observed in vivo. Although additional intermediate time points may further refine the kinetics of this transition, the current design consistently resolved distinct early and late output states across experimental systems.

Importantly, these temporal dynamics were strongly influenced by disease context. In 3×Tg mice, the transition toward maladaptive outputs occurred within a relatively short time frame, whereas in WT mice a delayed trajectory was observed. The inclusion of parallel WT time-course groups was therefore important for distinguishing general consequences of sustained STAT4 restoration from those shaped by the AD pathological environment. This divergence suggests that the disease background does not merely coexist with STAT4 signaling, but actively modifies how its downstream outputs emerge over time.

One plausible explanation for this context-dependent divergence is that the AD brain may represent a non-equilibrium signaling environment [4, 38, 39]. PI3K/AKT-related activity has often been reported to be relatively compromised in AD [38, 40–42], whereas ERK-related signaling is frequently elevated [43–45], indicating a shift in intracellular signaling balance. Notably, ERK/MAPK signaling has established roles in synaptic plasticity and learning-related processes [46, 47], but MAPK-related signaling has also been associated with neuronal stress and tau phosphorylation-related pathological contexts depending on upstream stimuli, timing, and disease state [48, 49]. Because STAT4 appears to positively influence both branches, its restoration may initially support neuronal stability, but in the AD context the same upstream input may progressively be redirected toward ERK-sensitive, stress- and apoptosis-associated outputs. In this framework, the late pathological phase does not necessarily indicate that STAT4 is intrinsically pathogenic; rather, it suggests that a disease-distorted signaling landscape biases its downstream consequences toward ERK-dominant maladaptive signaling. Although this interpretation remains inferential, it provides a biologically plausible explanation for why STAT4 restoration produces distinct output profiles across genotype, disease stage, and duration of restoration.

Consistent with this view, not all STAT4-associated outputs responded similarly to pathway modulation. ERK

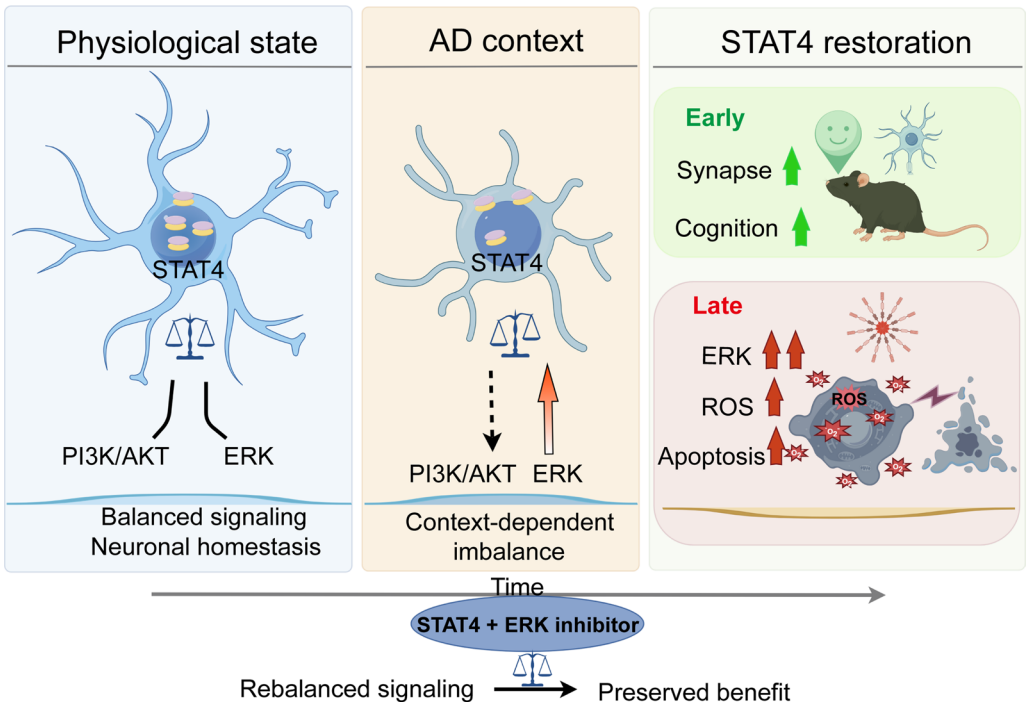

Fig. 9 A model of context-dependent STAT4 signaling in neuronal homeostasis and maladaptive responses in Alzheimer's disease

inhibition attenuated oxidative stress, apoptosis-related signaling, and tau-associated changes, supporting a functional role of ERK activity in mediating the late-stage pathological responses. By contrast, selected beneficial outputs, including reduced Aβ burden and improved synaptic and neuronal markers, remained detectable. To better understand this apparent divergence, we re-examined the integrated STAT4 Cut&Tag/RNA-seq analyses and further extracted STAT4-centered information from the STAT4-related WGCNA turquoise module. These analyses provided additional network-level clues. The integrated STAT4 Cut&Tag/RNA-seq analyses linked STAT4-bound and STAT4-responsive genes to neuronal/synaptic programs, including glutamatergic synapse and neuroactive ligand–receptor interaction, as well as intracellular signaling and stress-associated pathways, including PI3K-Akt, Ras/MAPK, and p53-related signaling. Further extraction of the WGCNA turquoise module identified STAT4-connected co-expression nodes related to amyloid biology, including APP and SORL1; tau-associated kinase/phosphatase regulation, including GSK3B, CDK5, MARK1, and PPP2CA; synaptic function, including SYP, GRIN2A, GRIN2B, and HOMER1; and oxidative stress, including SOD1. These pathway- and gene-level observations suggest that STAT4-associated signaling may be embedded in a broader network involving amyloid-related, synaptic, tau-associated kinase/phosphatase-related, and oxidative stress-related programs. This network-level relationship may help explain why amyloid burden, tau-associated stress responses, synaptic integrity, and behavioral outcomes do not change in a strictly linear manner. At the same time, these analyses do not identify a single direct APP- or MAPT-centered mechanism, and WGCNA-derived relationships represent co-expression network adjacency rather than directional or causal regulatory interactions. We therefore interpret these findings as network-level clues rather than evidence that STAT4 directly regulates amyloid or tau pathology.

Because ERK dependence was assessed pharmacologically in the present study, these findings are best interpreted as indicating that the late pathological outputs are, at least in part, ERK-sensitive, rather than exclusively controlled by ERK signaling. Importantly, these results do not imply complete mechanistic separation; instead, they suggest that distinct STAT4-associated outputs exhibit differential sensitivity to ERK modulation within a shared signaling framework. This pattern supports the possibility that beneficial and maladaptive consequences of STAT4 restoration may be at least partially uncoupled at the level of downstream signaling balance.

The behavioral data are broadly consistent with this interpretation and provide a possible explanation for why behavioral improvement can coexist with increased cell death-related markers. Behavioral performance likely reflects the integrated consequence of multiple

pathological and compensatory processes rather than a single molecular or histological readout. In the AD context, ERK inhibition alone was associated with modest behavioral effects, with a statistically significant improvement observed in MWM training, whereas the corresponding change in NOR did not reach significance. At the same time, sustained STAT4 overexpression at the later phase did not abolish behavioral benefit relative to vector-treated controls, but the magnitude of improvement was reduced compared with the earlier phase. This pattern suggests that prolonged STAT4 overexpression may preserve beneficial effects on neuronal and synaptic function while increasingly engaging late stress- and apoptosis-associated processes that constrain the net behavioral outcome. Under these conditions, combined STAT4 overexpression and ERK inhibition was associated with a more favorable late-phase behavioral trajectory than sustained STAT4 overexpression alone. In WT mice, the corresponding behavioral changes were weaker and did not reach significance over the time window examined here, consistent with a comparatively delayed or less pronounced behavioral divergence in the non-AD context. We therefore interpret the behavioral findings not as evidence that the observed effects are attributable exclusively to either intervention in isolation, but rather as a support for a model in which ERK inhibition can attenuate the late maladaptive component of sustained STAT4-associated signaling while beneficial outputs remain detectable. Within this framework, the rationale for combining STAT4 overexpression with ERK inhibition is not that ERK blockade is inert on its own [28, 45, 50], but that it may improve the late-phase balance of STAT4-associated outputs in the AD setting.

At the mechanistic level, we identified hnRNPK as a candidate STAT4-associated protein and showed that STAT4 is linked to intracellular signaling networks at both protein and transcript levels. hnRNPK was prioritized for further analysis because of its RNA-binding capacity [51–53] and dual nucleocytoplasmic localization [54, 55], both of which have been implicated in the regulation of mRNA stability and signaling dynamics in previous studies. The enrichment of STAT4-associated transcripts in PI3K/RAS/MAPK-related pathways further supports a role for coordinated regulation of signaling and RNA dynamics. At the same time, the interaction with hnRNPK should be regarded as a mechanistically informative component rather than a complete explanation of all downstream effects. Additional studies will be required to define the molecular architecture through which STAT4-associated regulation is translated into distinct signaling outputs over time.

An additional mechanistic issue concerns the restoration state of STAT4 itself. As a transcription factor, STAT4 function is unlikely to be determined solely by expression level and may also depend on post-translational regulation [56–58]. In the present study, we focused on the consequences of restoring STAT4 itself and the network-level outputs associated with that manipulation. However, in our preliminary modification-proteomics analysis using STAT4 immunoprecipitated from SH-SY5Y cell lysates, representative MS/MS spectra confirmed the presence of multiple modified forms of STAT4, including phosphorylation (Fig. S2f). These observations suggest that STAT4 activity in neuronal systems may be further shaped by modification-dependent state changes that influence localization, partner selection, or downstream transcriptional output. Because these regulatory layers were not systematically resolved here, the current work should be viewed as defining a functional role for STAT4-associated signaling in AD rather than fully establishing the modification code that governs STAT4 restoration under pathological conditions.

Several limitations should be acknowledged. First, although our data support a time-dependent shift in STAT4-associated outputs, the molecular events that drive the transition from adaptive to maladaptive signaling remain incompletely defined. Second, while ERK inhibition attenuated specific pathological readouts, the broader regulatory network is likely to extend beyond the PI3K/AKT-ERK axis examined here. Third, although consistent patterns were observed across cellular and animal models, further work will be required to determine how closely these findings reflect human disease progression and therapeutic responsiveness. Fourth, because ERK inhibition alone also influenced behavioral performance in the AD context, the relative contribution of STAT4-dependent and STAT4-independent components to specific behavioral outcomes will require further dissection. In addition, although the modification state of STAT4 is likely to be functionally important, this layer was not directly dissected in the present study. Finally, the present study analyzed only male mice in the in vivo experiments. Future studies including female mice will be needed to determine whether sex influences STAT4-associated signaling trajectories and behavioral outcomes in AD models.

Overall, our findings provide a framework for understanding how signaling dynamics shape neuronal outputs in AD. Rather than acting as a uniformly protective or uniformly pathogenic factor, STAT4 appears to function within a time-sensitive and context-sensitive signaling network in which prolonged restoration under AD conditions progressively favors ERK-sensitive maladaptive output. At the same time, selected beneficial outputs remain detectable, and their preservation under ERK inhibition

suggests that downstream rebalancing of signaling consequences may be feasible.

Within this framework, STAT4-driven signaling can be viewed as a dynamic and progressively rebalanced network in which early adaptive outputs and late ERK-sensitive maladaptive processes coexist and become uncoupled over time (Fig. 9). This conceptual model supports the view that therapeutic benefit may depend less on uniformly enhancing or suppressing STAT4-associated signaling than on selectively constraining its late maladaptive component while preserving earlier or parallel beneficial outputs. Together, these results support a model in which time-dependent signaling imbalance drives the progressive divergence of neuronal outcomes in AD.

Supplementary Information

The online version contains supplementary material available at https://doi.org/10.1186/s40035-026-00595-9.

Additional file 1. **Table S1** Primary antibodies used in this study

Additional file 2. **Table S2** Kits and reagents used in this study

Additional file 3. **Table S3** Summary of datasets, cell systems, animal models, species, and roles in the study

Additional file 4. **Table S4** Network-level clues linking STAT4-associated genes to neuronal/synaptic regulation, intracellular signaling, and tau phosphorylation-associated regulatory contexts.

Additional file 5. **Fig. S1**. Overview of the three snRNA-seq datasets. **Fig. S2**. Additional analyses supporting the association of STAT4 with PI3K/RAS/MAPK signaling.

Additional file 6. Uncropped gels and blots

Acknowledgements
The authors thank the Gene Expression Omnibus (GEO) database and the Gene Expression Profiling Interactive Analysis (GEPIA) platform for providing publicly available data and analytical resources.

Author contributions
J.T.L and P. C.W collaborated on the overall study design and coordinated the experiments. J.T.L performed cell culture, transfection, western blot experiments, analyzed all the data, created the figures and wrote the manuscript. L.C.C helped perform Golgi staining, animal behavioral tests and collected data. J.L helped perform Cut&Tag and IP-MS assay. Y.L.H helped perform and analyze RNA-seq. J.R.C helped perform RIP-seq assay. Y.J.F helped perform western blot experiments. H.X.M performed the ELISA assay. Y.L.H and S. G helped perform the immunostaining experiments. P. C.W supervised the project, evaluated analytical results, and reviewed the manuscript. All authors have read and approved the article.

Funding
This work was supported by the Beijing Natural Science Foundation (Grant No. L246009), the State Key Program of the National Natural Science Foundation of China (Grant No. 82030064), and the Beijing Municipal Health Commission Excellent Clinical Research Program of the Research Ward Parallel Project (Grant No. BRWEP2024W022010113).

Data availability
Publicly available datasets analyzed in this study are available from the Gene Expression Omnibus (GEO) under accession numbers GSE188545, GSE157827, GSE222007, GSE261596, GSE203206, and GSE159699. GTEx transcriptomic data used for correlation analyses were obtained from the Genotype-Tissue Expression (GTEx) Project. The high-throughput datasets generated in this study, including Cut&Tag, RNA-seq, IP-MS, and RIP-seq, are available from the corresponding author upon reasonable request.

Declarations

Ethics approval and consent to participate
Animal experiments were conducted in compliance with the guidelines and recommendations outlined in the Chinese Experimental Animals Administration Legislation. Animal studies were approved by the Ethics Committee of Xuanwu Hospital, Capital Medical University.

Consent for publication
Not applicable.

Competing interests
The authors declare that they have no competing interests.

Author details
[1]Department of Clinical Laboratory, Xuanwu Hospital, National Clinical Research Center for Geriatric Diseases, Capital Medical University, Beijing 100053, China.

Received: 29 April 2026 Accepted: 9 October 2026
Published online: 18 November 2026

References

1. Tzioras M, McGeachan RI, Durrant CS, Spires-Jones TL. Synaptic degeneration in Alzheimer disease. Nat Rev Neurol. 2023;19(1):19–38.
2. Dalal S, Ramirez-Gomez J, Sharma B, Devara D, Kumar S. MicroRNAs and synapse turnover in Alzheimer's disease. Ageing Res Rev. 2024;99:102377.
3. Peng L, Bestard-Lorigados I, Song W. The synapse as a treatment avenue for Alzheimer's disease. Mol Psychiatry. 2022;27(7):2940–9.
4. Kumari S, Dhapola R, Sharma P, Paidlewar M, Vellingiri B, Medhi B, et al. Unravelling neuronal death mechanisms: the role of cytokines and chemokines in immune imbalance in Alzheimer's disease progression. Ageing Res Rev. 2025;112:102883.
5. Iatrou A, Clark EM, Wang Y. Nuclear dynamics and stress responses in Alzheimer's disease. Mol Neurodegener. 2021;16(1):65.
6. Alqahtani SM, Al-Kuraishy HM, Al-Gareeb AI, Albuhadily AK, Shokr MM, Alexiou A, et al. Pharmacological modulation of the PI3K/AKT/GSK3β axis: a new frontier in Alzheimer's disease treatment. Inflammopharmacology. 2026;34(1):267–83.
7. Ritchie EM, Jin Y. Context specificity of MAP3K DLK signaling in the nervous system: insights from genetics and genomics. Annu Rev Genet. 2025;59(1):189–213.
8. Calakos N, Caffall ZF. The integrated stress response pathway and neuromodulator signaling in the brain: lessons learned from dystonia. J Clin Invest. 2024;134(7):e177833.
9. Shi Z, Wen K, Sammudin NH, LoRocco N, Zhuang X. Erasing "bad memories": reversing aberrant synaptic plasticity as therapy for neurological and psychiatric disorders. Mol Psychiatry. 2025;30(7):3209–25.
10. Krugers HJ, Joëls M. The stress response is adaptive in a context- and state-dependent manner. Cells. 2025;14(24):1957.
11. Tang L, Liu F, Sun X, Yang J, Liu Y, Pan X, et al. The Janus face of CaMKII: from memory consolidation to neurotoxic switch in Alzheimer's disease. Arch Toxicol. 2025;99(12):4829–68.
12. Soelter TM, Howton TC, Clark AD, Oza VH, Lasseigne BN. Altered glia-neuron communication in Alzheimer's disease affects WNT, p53,

and NFkB signaling determined by snRNA-seq. Cell Commun Signal. 2024;22(1):317.
13. Sheehan PW, Fass SB, Sapkota D, et al. A glial circadian gene expression atlas reveals cell-type and disease-specific reprogramming in response to amyloid pathology or aging. Nat Neurosci. 2025;28(11):2366–79.
14. Sarapultsev A, Gusev E, Komelkova M, Utepova I, Luo S, Hu D. JAK-STAT signaling in inflammation and stress-related diseases: implications for therapeutic interventions. Mol Biomed. 2023;4(1):40.
15. Clark DN, Brown SV, Xu L, Lee RL, Ragusa JV, Xu Z, et al. Prolonged STAT1 signaling in neurons causes hyperactive behavior. Brain Behav Immun. 2025;124:1–8.
16. Li Y, Ma W, Ma R, Wang S, Liu X, Guo X, et al. FMRP regulation of STAT3-MYC signaling is critical for adult hippocampal neurogenesis and cognitive flexibility. Cell Death Differ. 2026;33(1):200–18.
17. Yang C, Mai H, Peng J, Zhou B, Hou J, Jiang D. STAT4: an immunoregulator contributing to diverse human diseases. Int J Biol Sci. 2020;16(9):1575–85.
18. Madera-Salcedo IK, Ramírez-Sánchez AL, Rodríguez-Rodríguez N, García-Quintero R, Rubio RM, Morales-Montes de Oca G, et al. Down-regulation-resistant STAT4 risk haplotype contributes to lupus nephritis through CD4+ T cell interferon-γ production. Arthritis Rheumatol. 2023;75(6):961–72.
19. Zhang YS, Xin DE, Wang Z, Peng W, Zeng Y, Liang J, et al. Acetylation licenses Th1 cell polarization to constrain *Listeria monocytogenes* infection. Cell Death Differ. 2022;29(11):2303–15.
20. Jin W, Pei J, Roy JR, Jayaraman S, Ahalliya RM, Kanniappan GV, et al. Comprehensive review on single-cell RNA sequencing: a new frontier in Alzheimer's disease research. Ageing Res Rev. 2024;100:102454.
21. Luquez T, Gaur P, Kosater IM, Lam M, Lee DI, Mares J, et al. Cell type-specific changes identified by single-cell transcriptomics in Alzheimer's disease. Genome Med. 2022;14(1):136.
22. Mathys H, Peng Z, Boix CA, Victor MB, Leary N, Babu S, et al. Single-cell atlas reveals correlates of high cognitive function, dementia, and resilience to Alzheimer's disease pathology. Cell. 2023;186(20):4365–4385.e27.
23. Chen C, Wang J, Pan D, Wang X, Xu Y, Yan J, et al. Applications of multi-omics analysis in human diseases. MedComm (2020). 2023;4(4):e315.
24. Liu X, Peng T, Xu M, Lin S, Hu B, Chu T, et al. Spatial multi-omics: deciphering technological landscape of integration of multi-omics and its applications. J Hematol Oncol. 2024;17(1):72.
25. Gossen M, Bujard H. Tight control of gene expression in mammalian cells by tetracycline-responsive promoters. Proc Natl Acad Sci U S A. 1992;89(12):5547–51.
26. Langfelder P, Horvath S. WGCNA: an R package for weighted correlation network analysis. BMC Bioinformatics. 2008;9:559.
27. Zhang B, Horvath S. A general framework for weighted gene co-expression network analysis. Stat Appl Genet Mol Biol. 2005;4:Article17.
28. Xiong Y, Yang Y, Ruan Y, Ou W, Hu Z, Li W, et al. Magnesium-L-threonate ameliorates cognitive deficit by attenuating adult hippocampal neurogenesis impairment in a mouse model of Alzheimer's disease. Exp Neurobiol. 2025;34(2):53–62.
29. Zhang J, Liu C, Liu J, Cui Y, Hou Y, Song Q, et al. The autocrine motility factor receptor delays the pathological progression of Alzheimer's disease via regulating the ubiquitination-mediated degradation of APP. Alzheimers Res Ther. 2025;17(1):95.
30. Sawangjit A, Oyanedel CN, Niethard N, Salazar C, Born J, Inostroza M. The hippocampus is crucial for forming non-hippocampal long-term memory during sleep. Nature. 2018;564(7734):109–13.
31. Cui Y, Zhang X, Liu J, Hou Y, Song Q, Cao M, et al. Myeloid ectopic viral integration site 2 accelerates the progression of Alzheimer's disease. Aging Cell. 2024;23(10):e14260.
32. Wang Y, Cui Y, Liu J, Song Q, Cao M, Hou Y, et al. Krüppel-like factor 5 accelerates the pathogenesis of Alzheimer's disease via BACE1-mediated APP processing. Alzheimers Res Ther. 2022;14(1):103.
33. Hou Y, Song Q, Wang Y, Liu J, Cui Y, Zhang X, et al. Downregulation of Krüppel-like factor 14 accelerated cellular senescence and aging. Aging Cell. 2023;22(10):e13950.
34. Sharma V, Kaur A, Singh TG. Counteracting role of nuclear factor erythroid 2-related factor 2 pathway in Alzheimer's disease. Biomed Pharmacother. 2020;129:110373.
35. Hashimoto K, Chen SJ, Fujio K, Kayama A, Sugimoto N, Takayama N, et al. STAT1-mediated epigenetic regulation of LIN28A controls iPSC-derived platelet production through the let-7-RALB axis. Blood Adv. 2025;9(17):4345–56.
36. Meng X, Liu Z, Zhao Z, Chen L, Li S, Song Q, et al. Trans-activator of transcription-pre-B-cell leukemia transcription factor 1 alleviates Alzheimer's disease by reducing neuronal insulin resistance and restoring energy homeostasis. Neural Regen Res. 2026;21(9):4390–405.
37. Mémet S. NF-kappaB functions in the nervous system: from development to disease. Biochem Pharmacol. 2006;72(9):1180–95.
38. Kumari S, Dhapola R, Reddy DH. Apoptosis in Alzheimer's disease: insight into the signaling pathways and therapeutic avenues. Apoptosis. 2023;28(7–8):943–57.
39. Chavoshinezhad S, Beirami E, Izadpanah E, Feligioni M, Hassanzadeh K. Molecular mechanism and potential therapeutic targets of necroptosis and ferroptosis in Alzheimer's disease. Biomed Pharmacother. 2023;168:115656.
40. Kirouac L, Rajic AJ, Cribbs DH, Padmanabhan J. Activation of Ras-ERK signaling and GSK-3 by amyloid precursor protein and amyloid beta facilitates neurodegeneration in Alzheimer's disease. eNeuro. 2017;4(2):ENEURO-0149.
41. Song Z, He C, Yu W, Yang M, Li Z, Li P, et al. Baicalin attenuated Aβ (1-42)-induced apoptosis in SH-SY5Y cells by inhibiting the Ras-ERK signaling pathway. BioMed Res Int. 2022;2022:9491755.
42. Li Z, Yin B, Zhang S, Lan Z, Zhang L. Targeting protein kinases for the treatment of Alzheimer's disease: recent progress and future perspectives. Eur J Med Chem. 2023;261:115817.
43. Huang J, Xu Z, Yu C, Liu L, Ji L, Qiu P, et al. The volatile oil of *Acorus tatarinowii* Schott ameliorates Alzheimer's disease through improving insulin resistance via activating the PI3K/AKT pathway. Phytomedicine. 2024;135:156168.
44. Qi W, Ying Y, Wu P, Dong N, Fu W, Liu Q, et al. Inhibition of miR-4763-3p expression activates the PI3K/mTOR/Bcl2 autophagy signaling pathway to ameliorate cognitive decline. Int J Biol Sci. 2024;20(15):5999–6017.
45. Wu L, Sun Y, Yin Y, Wu Z, Liu R, Liu Y, et al. Lancao decoction in the treatment of Alzheimer's disease via activating PI3K/AKT signaling to promote ERK involving in enhancing neuronal activities in the hippocampus. J Ethnopharmacol. 2025;338(Pt 1):119017.
46. Thomas GM, Huganir RL. MAPK cascade signalling and synaptic plasticity. Nat Rev Neurosci. 2004;5(3):173–83.
47. English JD, Sweatt JD. A requirement for the mitogen-activated protein kinase cascade in hippocampal long term potentiation. J Biol Chem. 1997;272(31):19103–6.
48. Ferrer I, Blanco R, Carmona M, Ribera R, Goutan E, Puig B, et al. Phosphorylated Map kinase (ERK1, ERK2) expression is associated with early tau deposition in neurones and glial cells, but not with increased nuclear DNA vulnerability and cell death, in Alzheimer disease, Pick's disease, progressive supranuclear palsy and corticobasal degeneration. Brain Pathol. 2001;11(2):144–58.
49. Veeranna, Kaji T, Boland B, Odrljin T, Mohan P, Basavarajappa BS, et al. Calpain mediates calcium-induced activation of the erk1,2 MAPK pathway and cytoskeletal phosphorylation in neurons: relevance to Alzheimer's disease. Am J Pathol. 2004;165(3):795–805.
50. Wang X, Wang Y, Zhu Y, Yan L, Zhao L. Neuroprotective effect of S-trans, trans-farnesylthiosalicylic acid via inhibition of RAS/ERK pathway for the treatment of Alzheimer's disease. Drug Des Devel Ther. 2019;13:4053–63.
51. Bampton A, Gatt A, Humphrey J, Cappelli S, Bhattacharya D, Foti S, et al. HnRNP K mislocalisation is a novel protein pathology of frontotemporal lobar degeneration and ageing and leads to cryptic splicing. Acta Neuropathol. 2021;142(4):609–27.
52. Song Y, Liu Y, Chi R, Wang P, Di R, He X, et al. Study on the mechanism of LNC004268 regulating sheep myoblast proliferation and differentiation through hnRNPK-CNOT2 axis. Int J Biol Macromol. 2025;321(Pt 4):146625.
53. Tang Y, Zhao B, Wang W, Chen H, Zhang J, Xie Y, et al. The EGR1-mediated lncRNA TENM3-AS1 potentiates gastric cancer metastasis via reprogramming fatty acid metabolism. Mol Cancer. 2025;24(1):165.
54. Gao H, Yang S, Ning A, Yin L, Lan Y, Cheng K, et al. Azoospermia phenotype and scRNA-seq reveal hnRNPK as a factor essential for male germ cell development in mice. Nucleic Acids Res. 2026;54(4):gkag108.
55. Mucha B, Qie S, Bajpai S, Tarallo V, Diehl JN, Tedeschi F, et al. Tumor suppressor mediated ubiquitylation of hnRNPK is a barrier to oncogenic translation. Nat Commun. 2022;13(1):6614.

56. Brovchenko N, Berg A, Schubert S, Gräb J, Münzel T, Protzel C, et al. Biaryl phosphates and phosphonates as selective inhibitors of the transcription factor STAT4. Angew Chem Int Ed Engl. 2025;64(21):e202504420.
57. Xia Y, Xie Y, Zhang H, Liu L. STAT4 gene polymorphisms in human diseases. Front Immunol. 2024;15:1479418.
58. Wang QW, Sun LH, Zhang Y, Wang Z, Zhao Z, Wang ZL, et al. MET overexpression contributes to STAT4-PD-L1 signaling activation associated with tumor-associated, macrophages-mediated immunosuppression in primary glioblastomas. J Immunother Cancer. 2021;9(10):e002451.